Biochemistry

pubs.acs.org/biochemistry Article

Rapid ^{2}H NMR Transverse Relaxation of Perdeuterated Lipid Acyl Chains of Membrane with Bound Viral Fusion Peptide Supports Large-Amplitude Motions of These Chains That Can Catalyze Membrane Fusion

Ujjayini Ghosh and David P. Weliky*

Cite This: *Biochemistry* 2021, 60, 2637−2651 Read Online

ACCESS | Metrics & More | Article Recommendations | Supporting Information

ABSTRACT: An early step in cellular infection by a membrane-enveloped virus like HIV or influenza is joining (fusion) of the viral and cell membranes. Fusion is catalyzed by a viral protein that typically includes an apolar "fusion peptide" (fp) segment that binds the target membrane prior to fusion. In this study, the effects of nonhomologous HIV and influenza fp's on lipid acyl chain motion are probed with ^{2}H NMR transverse relaxation rates (R_2's) of a perdeuterated DMPC membrane. Measurements were made between 35 and 0 °C, which brackets the membrane liquid-crystalline-to-gel phase transitions. Samples were made with either HIV "GPfp" at pH 7 or influenza "HAfp" at pH 5 or 7. GPfp induces vesicle fusion at pH 7, and HAfp induces more fusion at pH 5 vs 7. GPfp bound to DMPC adopts an intermolecular antiparallel β sheet structure, whereas HAfp is a monomer helical hairpin. The R_2's of the no peptide and HAfp, pH 7, samples increase gradually as temperature is lowered. The R_2's of GPfp and HAfp, pH 5, samples have very different temperature dependence, with a ∼10× increase in R_2^{CD2} when temperature is reduced from 25 to 20 °C and smaller but still substantial R_2's at 10 and 0 °C. The large R_2's with GPfp and HAfp, pH 5, are consistent with large-amplitude motions of lipid acyl chains that can aid fusion catalysis by increasing the population of chains near the aqueous phase, which is the chain location for transition states between membrane fusion intermediates.

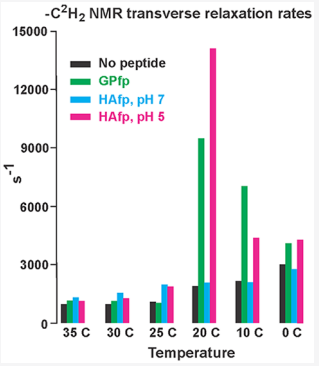

Many zoonotic pathogens like human immunodeficiency virus (HIV), influenza virus, and coronaviruses are membrane-enveloped viruses. An early step in infection by these viruses is joining (fusion) of the viral and target cell membranes.[1−5] Fusion is catalyzed by a viral protein that is specific to each virus family and which typically has a N-terminal receptor-binding subunit (RbSu) and C-terminal fusion subunit (FsSu). The RbSu binds to specific (to the virus) molecules in a target cell membrane, followed by separation of the RbSu from the FsSu, and then catalysis of membrane fusion by the FsSu. The FsSu is typically a monotopic integral membrane protein of the virus with a substantial N-terminal ectodomain (Ed) outside the virus. HIV, influenza, and coronaviruses all have "class I" fusion proteins, for which the Ed's of three FsSu's form a complex with three RbSu's.[1] After receptor-binding and RbSu separation, there is substantial structural change of much of the three FsSu Ed's to a thermostable trimer-of-hairpins structure. The N-terminal region of the FsSu Ed is not part of the hairpin, and a ∼25-residue segment in this region is called the "fusion peptide" (fp) and is thought to bind the target membrane during fusion (Figure 1A,E).[6] The fp segment is typically a conserved sequence with apolar residues and defined structure in detergent and/or membrane and exhibits mutations that disrupt FsSu-mediated fusion.[4,5,7−21] For the HIV glycoprotein (GP) 41 kDa and influenza hemagglutinin (HA) subunit 2 FsSu's, the consensus fp's are at the N-termini of the respective FsSu's, with GPfp and HAfp sequences presented in Figure 2B.

The present study is an investigation of the effects of GPfp and HAfp on lipid acyl chain motion via measurement of ^{2}H NMR transverse relaxation rates (R_2's) of dimyristoylphosphatidylcholine lipid with perdeuterated acyl chains (DMPC-d54, Figure 2A). The R_2 has the greatest contribution from "slow" motions, which have significant spectral density at frequencies <100 kHz.[22−26] The R_2 depends both on the mean-squared variation of the ^{2}H quadrupolar NMR frequency due to slow motions and the spectral density in the low-frequency regime. The temperature dependence of R_2 is interesting, because lowering temperature has countervailing effects of decreasing amplitudes and increasing the spectral density of slow-frequency motions. The samples of this study contain

Received: May 4, 2021
Revised: August 13, 2021
Published: August 26, 2021

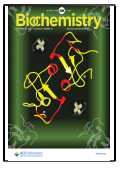

https://doi.org/10.1021/acs.biochem.1c00316
Biochemistry 2021, 60, 2637−2651

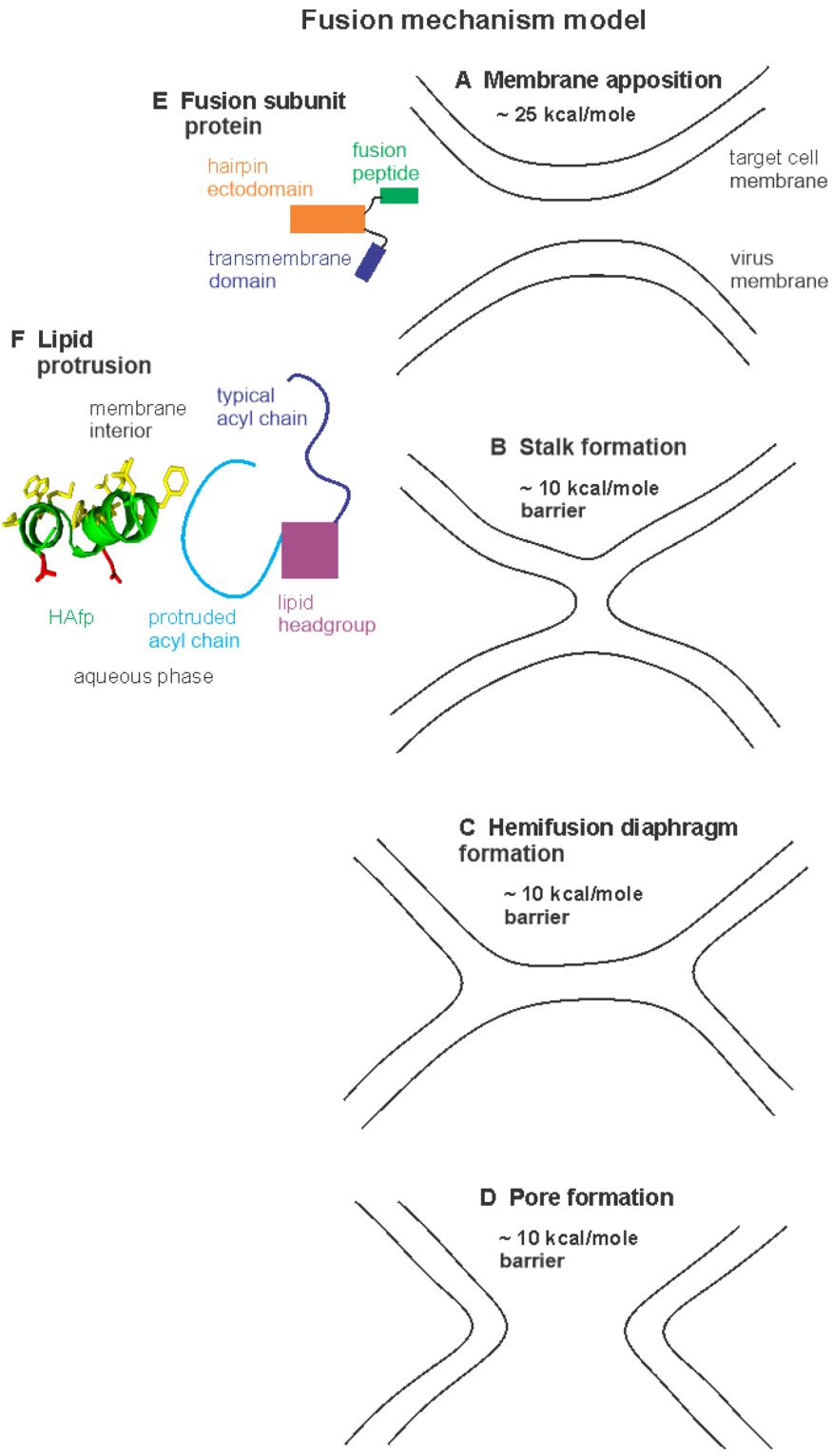

Figure 1. Fusion mechanism model. Panels A–D display membrane states during fusion. In the absence of fusion subunit protein, calculations suggest that ~25 kcal/mol of energy is required to closely appose two membranes and that there are ~10 kcal/mol barriers to formation of each of the three subsequent states. The membrane apposition energy may be reduced by the thermostable hairpin structure of the soluble ectodomain of the viral fusion protein subunit in conjunction with the fusion peptide bound to the target membrane and the transmembrane domain in the viral membrane (panel E). Both monomer and trimer forms of the hairpin have been reported, and the trimer would have three fusion peptides and three transmembrane domains. The barrier for the apposed membranes → stalk step (A → B) may be reduced by perturbation of the acyl chains of the target membrane lipids near the fusion peptide. Panel F shows a schematic model of one type of perturbation that is suggested by molecular dynamics simulations of membrane with monomer HAfp. These simulations show larger motional amplitudes and higher probability of protrusion, i.e., location of the lipid acyl chain closer to the aqueous phase. The HAfp in panel F is represented as the semiclosed helical hairpin structure located in the outer leaflet of the target cell membrane with some hydrophobic side chains in the membrane interior and some polar side chains in the aqueous phase.

https://doi.org/10.1021/acs.biochem.1c00316
Biochemistry 2021, 60, 2637–2651

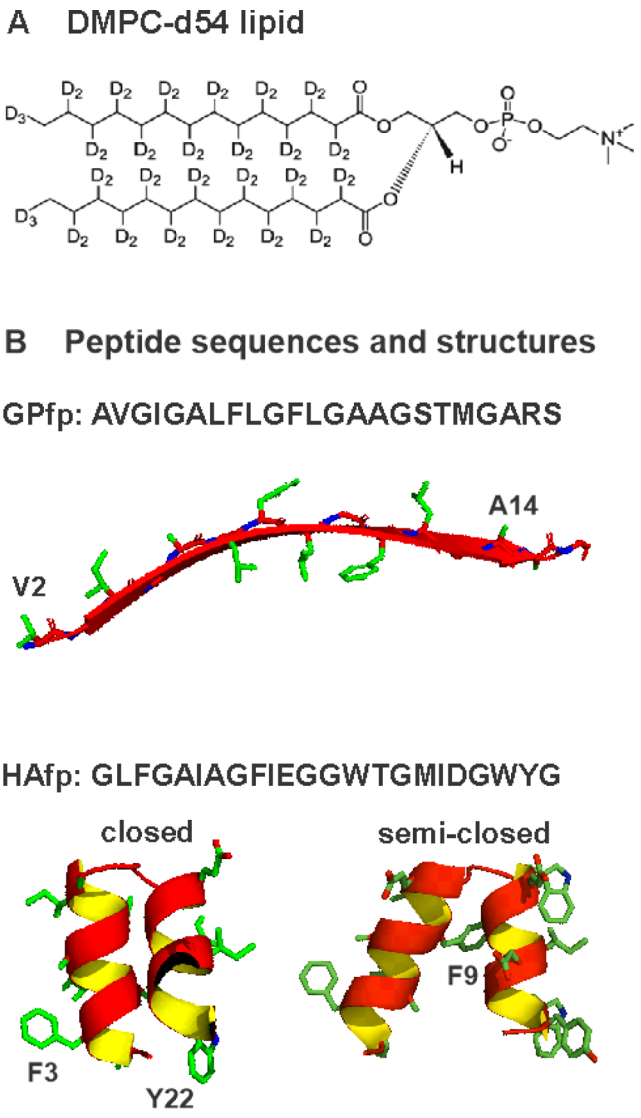

Figure 2. Panel A displays the chemical structure of DMPC-d54 lipid with D ≡ ^{2}H. Panel B displays sequences and structural models of GPfp and HAfp based on data for peptide without the rest of the protein. A few residues are identified in the models. One strand of a GPfp intermolecular antiparallel β sheet is displayed. The sheets have distributions of adjacent strand registries that include the residue 1 → 16/16 → 1 and 1 → 17/17 → 1 registries. HAfp is a monomeric helical hairpin with populations of closed and semiclosed structures. The closed structure is based on PDB 2KXA.

membrane with only DMPC-d54, in part to take advantage of defined but different predominant structures for GPfp and HAfp in this single lipid (Figure 2B).[27] GPfp is an oligomer and adopts intermolecular antiparallel β sheet structure, whereas HAfp is a monomer and adopts α helical hairpin structures.[12,14,18] The number of GPfp in an oligomer is likely fairly small, e.g., <20.[21] Other structures are adopted by GPfp and HAfp when they are bound to environments other than DMPC. For example, GPfp adopts a predominant monomeric α helical structure in detergent-rich media, whereas in membrane with 30 mol % cholesterol, HAfp adopts a predominant oligomeric β sheet structure.[11,28−30] The use of a single-component DMPC-d54 membrane in the present study allows comparison of the effects on lipids of the two nonhomologous GPfp and HAfp sequences as well as the different intermolecular β and monomer α structures with the goal of discerning fp effects on membrane that are more universal. There is also evidence that the GPfp and HAfp structures are retained for the fp's in much larger constructs that include the Ed hairpin.[16,17,31−33]

Samples with GPfp are prepared at neutral pH, which matches the pH of HIV/cell fusion, whereas samples with HAfp are prepared at both pH 5 and 7.[34−36] Fusion of influenza virus happens within late endosomes for which pH ≈ 5.[1] The GPfp with the oligomeric β structure induces substantial vesicle fusion at pH 7, whereas HAfp with a helical hairpin structure induces higher vesicle fusion at pH 5 vs 7, which also matches the pH dependence of vesicle fusion by large HA2 constructs that include HAfp.[18,20,37,38] Several groups have investigated the basis for why HAfp is more "fusogenic" at pH 5 vs 7, but there is not yet a consensus on the mechanism for the pH difference.[18,39−42] It has been shown that HAfp in membrane adopts two variants of the helical hairpin structure, closed and semiclosed (Figure 2B), and there is a larger semiclosed fraction at pH 5 vs 7.[15,18]

Figure 1 displays one model of the fusion mechanism that illustrates potential contributions of the fp to fusion. In the absence of FsSu, there is a ∼25 kcal/mol calculated barrier to the membrane apposition step, which precedes fusion (Figure 1A,E).[2] This barrier could be reduced by fp binding to the target membrane in conjunction with the thermostable hairpin structure of the C-terminal Ed region of the FsSu.[20,38,43,44] The barrier could be further lowered by membrane dehydration induced by fp.[45] Apposition is followed by "stalk" and then "hemifusion diaphragm" intermediates, which are respectively contiguous with the outer and inner leaflets of the two fusing bodies (Figure 1B,C).[2,4,34,46] Small pores are formed, at least one pore expands so that the diaphragm is eliminated, and there is a resultant single contiguous membrane and compete mixing of contents of the two bodies (Figure 1D). In the absence of FsSu, there are ∼10 kcal/mol calculated barriers between the apposition → stalk, stalk → hemifusion, and hemifusion → fusion pore structures.[2] The barriers exist in part because lipids have to move through transient configurations with energies higher than those of a typical membrane bilayer, e.g., moving a small group of lipids through water to form a new leaflet in a new bilayer. One way the membrane-bound fp could reduce these barriers is by increasing amplitudes of lipid thermal motions with accompanying larger populations of configurations that are closer to those of the transition-state geometries. There are both data that support increased motional amplitudes with fp and data that support decreased amplitudes, so the fp effect on lipid motions remains unresolved.

Experimental support for increased amplitudes includes narrower ^{2}H NMR spectra for DMPC-d54 with vs without fp.[27] Spectra were also obtained over a range of temperatures that spanned the liquid-crystalline and gel phases of the lipid, and relative to without fp, comparable spectral lineshapes and linewidths with fp were obtained at 10−20 °C lower temperature. These effects were observed with HAfp at pH 5 or with GPfp at pH 7, which respectively adopt a monomeric helical hairpin or oligomeric β sheet structure (Figure 2B). By contrast, there were comparable lineshapes and linewidths for no peptide and HAfp at pH 7, where less fusion is induced. The frequency differences between "horns" in the liquid-crystalline spectra are proportional to the order parameters $S_n = \langle(3\cos^2\theta_n - 1)/2\rangle$, with $0 \le S_n \le 1$ where n is the index for

https://doi.org/10.1021/acs.biochem.1c00316
Biochemistry 2021, 60, 2637−2651

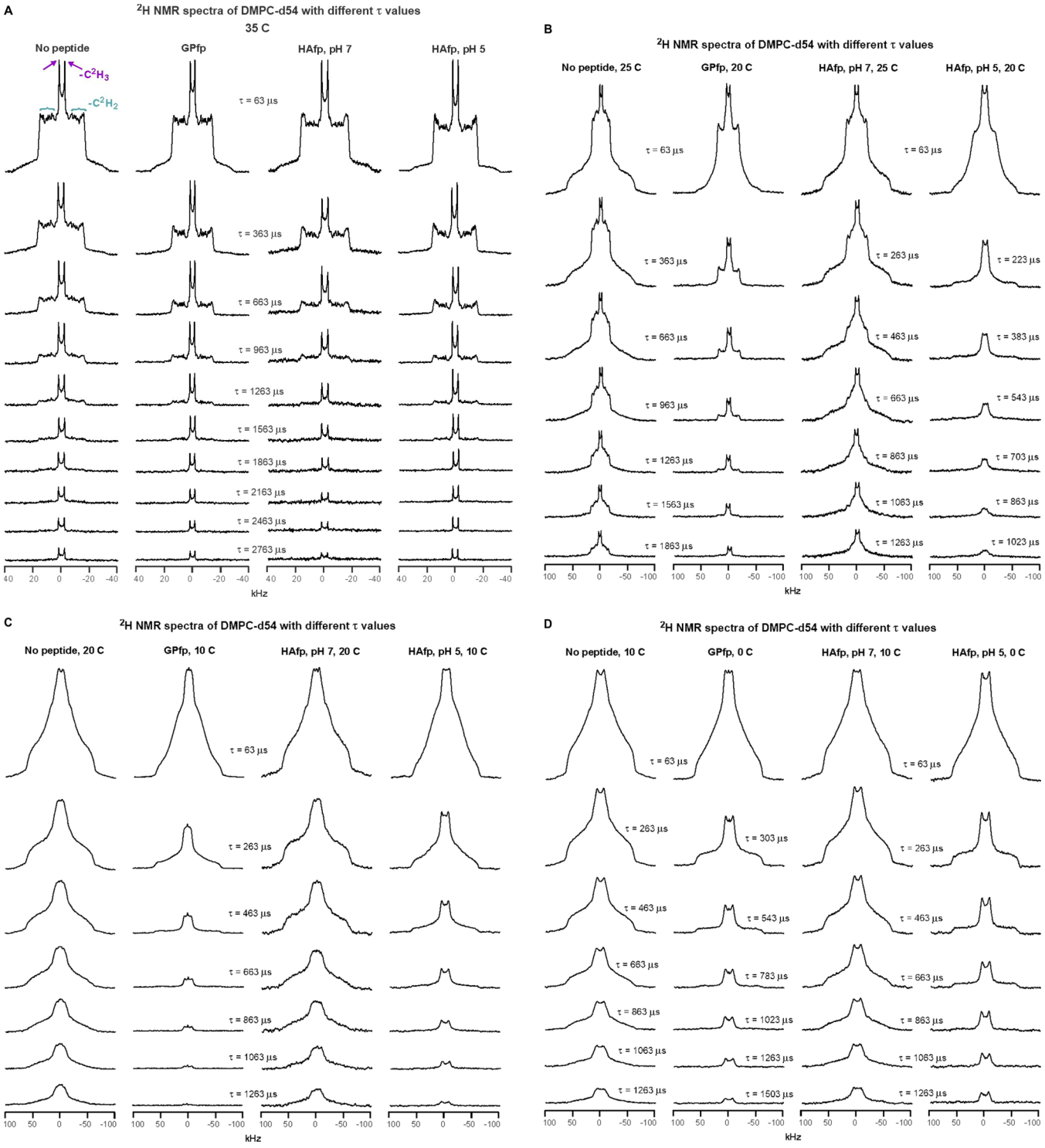

Figure 3. ^{2}H NMR spectra of samples with DMPC-d54 at different temperatures and different relaxation times $\equiv \tau$. The pulse sequence is the solid-echo sequence $\pi/2-\tau_a-\pi/2-\tau_b-$ acquisition so that $\tau = \tau_a + \tau_b + 22$ μs. Each sample contained either DMPC-d54 without peptide (left columns) or DMPC-d54 with peptide and peptide:DMPC-d54 = 1:25 molar ratio (right columns). For each of the (A–D) panels, the displayed spectra have similar lineshapes for the shortest-time $\tau = 63$ μs spectra. This similarity indicates similar order parameters of the four samples and similar amplitudes of motions with frequencies >100 kHz. For the same column within a panel, each spectrum is the sum of the same number of scans, where 500 is a typical number. For the same column within a panel, each spectrum is processed with the same exponential line broadening, and the typical broadening is 100 Hz for panel A, 500 Hz for panel B, and 1000 Hz for panels C and D. The $-C^2H_3$ "horns" and $-C^2H_2$ horn regions are identified for the 35 °C no peptide spectrum at the shortest τ, where the horns are peaks corresponding to the most probable $\theta = 90°$ orientation with respect to the NMR field.

a particular acyl chain carbon, θ_n is the angle between the C_n-^2H bond and the NMR magnetic field, and $\langle\cdots\rangle$ is the average over "fast" motions whose frequencies are >100 kHz.[26] At 35 °C and a 1:25 peptide:lipid ratio, the order parameters

https://doi.org/10.1021/acs.biochem.1c00316
Biochemistry 2021, 60, 2637–2651

for GPfp and HAfp, pH 5, are respectively ∼15 and ∼8% narrower/smaller than no peptide and for HAfp, pH 7, are ∼4% broader/larger. At a 1:50 ratio, the magnitudes of the changes are smaller, i.e., the spectra with peptide become more similar to no peptide. Larger-amplitude lipid motions are also observed in several molecular dynamics simulations for membrane with monomer HAfp, with highest amplitudes for lipids close to an HAfp.[47−49] There is semiquantitative agreement between the NMR- and simulation-derived reductions in order parameters for lipid with HAfp, pH 5, and also agreement between NMR- and X-ray-scattering-derived reductions for lipid with GPfp.[27,47−50] For the simulations, the increased motions result in acyl chain protrusion into the aqueous phase and headgroup intrusion into the hydrocarbon interior of the bilayer, i.e., a partial rotation of the lipid molecule that is along the reaction coordinate between topologically distinct fusion intermediates.[4,47−49,51] In the present study, these simulation and other data are used to interpret large differences in experimental ^{2}H NMR R_2's of lipid with vs without fp, with resulting improved understanding of the fp contribution to membrane fusion.

MATERIALS AND METHODS

Materials. GPfp has the sequence AVGIGALFLGFLGAA-GSTMGARSWKKKKKKG, and HAfp has the sequence GLFGAIAGFIEGGWTGMIDGWYGGKKKKG, and the underlined residues are respectively the N-terminal residues of the HIV gp41 and the influenza virus HA2 proteins. The GPfp sequence is from the LAV-1 laboratory strain of HIV, and the HAfp sequence is an H1 serotype. The C-terminal, nonunderlined residues are non-native. The G and K residues increase aqueous solubility, and the W in GPfp is a 280 nm absorption chromophore. Synthesis and purification have been previously described.[27] DMPC-d54 lipid was purchased from Avanti Polar Lipids (Alabaster, Al). Buffers were 10 mM HEPES and 5 mM MES adjusted to either pH 5.0, 7.0, or 7.4 and contained 0.01% sodium azide as preservative.

NMR Sample Preparation. The sample preparation has been previously described and reliably results in HAfp with helical hairpin and GPfp with β sheet structures.[27] Briefly, the "no peptide" lipid film was prepared by dissolving dry DMPC-d54 in chloroform:methanol (9:1), followed by solvent removal with nitrogen gas and overnight vacuum. The film was suspended in water, subjected to multiple freeze/thaw cycles, and extruded through a 100 nm diameter polycarbonate filter to form large unilamellar vesicles (LUVs). The LUV suspension was ultracentrifuged, and the pellet was harvested, lyophilized, transferred to a 4 mm diameter NMR rotor, and hydrated with ∼20 μL of water. Samples with peptide were typically prepared with a 1:25 peptide:DMPC-d54 molar ratio. For HAfp samples, DMPC-d54 LUV's were prepared in buffer at either pH 5.0 or 7.0 and subjected to dropwise addition of a HAfp solution while maintaining pH. The HAfp + LUV suspension was then treated similarly to the no peptide except that hydration was done with buffer that maintained the pH of the sample. Preparation of GPfp and DMPC-d54 began with codissolution in 2,2,2-trifluoroethanol:chloroform:1,1,1,3,3,3-hexafluoroisopropanol (2:3:2) followed by solvent removal with by nitrogen gas and overnight vacuum. The peptide + lipid film was treated similarly to the no peptide film except that there was not extrusion and buffer at pH 7.4 was used.

NMR Spectroscopy and Data Analysis. ^{2}H NMR spectra were acquired on a 9.4 T Infinity Plus spectrometer using a probe equipped for 4 mm diameter rotors. Nitrogen gas at defined temperature was flowed around the sample for ∼1 h prior to data acquisition, and spectra were then obtained with T_{N2} between 35 and 0 °C, which brackets the ∼20 and ∼10 °C temperatures of the respective $L_\alpha \rightarrow P_{\beta'}$ transition and $P_{\beta'} \rightarrow L_{\beta'}$ phase transitions of hydrated DMPC-d_{54}, with $L_\alpha \equiv$ liquid-crystalline, $P_{\beta'} \equiv$ rippled gel, and $L_{\beta'} \equiv$ gel phase.[52] ^{2}H NMR spectra were acquired without spinning and with the solid-echo pulse sequence $(\pi/2)_x-\tau_a-(\pi/2)_y-\tau_b-$acquire. Typical parameters included 61.5 MHz transmitter frequency, 1.6 μs $\pi/2$ pulse (calibrated with ^2H_2O), dwell time = 2 μs, recycle delay = 1 s, and acquisition of a few hundred to a few thousand scans. Data processing included removal of the first 11 points ≡22 μs so that the initial time is the peak echo, as well as exponential line broadening, Fourier transformation, phasing, and dc offset correction. For each sample at a particular temperature, data were acquired for an array of $\tau_{a,k}$ and $\tau_{b,k}$ values with typical $\tau_{a,k} = 30\ \mu s + (k \times \Delta\tau/2)$, $\tau_{b,k} = 11\ \mu s + (k \times \Delta\tau/2)$, and $k = 0, 1, 2, \ldots k_{max}$. The NMR signal decay includes terms with $\exp(-R_2 \times \tau_k)$ dependence where $\tau_k = 63\ \mu s + (k \times \Delta\tau)$. The $\Delta\tau$ and k_{max} values were selected to allow accurate determination of the R_2's.

Each processed spectrum contained a central region that had contributions from the narrower $-C^2H_3$ powder pattern and the broader $-C^2H_2$ powder patterns and also outlying regions that only had contributions from the $-C^2H_2$ powder patterns (Figure S1). For each set of spectra of a sample at one temperature, the integrated $-C^2H_3$ intensity (I^{CD3}) was typically calculated using the difference between integration over the central spectral region with $-C^2H_3$ and $-C^2H_2$ contributions and integration over nearby ranges that only contained $-C^2H_2$ contributions, i.e., $I^{CD3} = {}_{-\nu 1}\int^{\nu 1} I(\nu)\ d\nu - {}_{\nu 2}\int^{\nu 3} I(\nu)\ d\nu + {}_{-\nu 2}\int^{-\nu 3} I(\nu)\ d\nu$, with $|\nu_1| = |(\nu_3 - \nu_2)|$. Integration over the full $-C^2H_3$ spectral width for ${}_{-\nu 1}\int^{\nu 1} I(\nu)\ d\nu$ was achieved with $\nu_1 \approx \Delta\nu_{CD3}$, where $\Delta\nu_{CD3}$ is the frequency difference between the prominent innermost "horns" of a spectrum that correspond to the most likely $\theta = 90°$ orientation of the $-C^2H_3$ group with respect to the NMR field (Figures 3A and S1).[26] The $I^{CD2,inner}$ was calculated by integration over the $(\nu_2 \rightarrow \nu_3) + (-\nu_2 \rightarrow -\nu_3)$ regions, and $I^{CD2,outer}$ was calculated by integration over symmetric frequency ranges in the more outlying regions of the spectrum. The specific frequency values for the integration ranges varied with sample and temperature, because the spectral lineshapes and linewidths strongly depended on sample and temperature (Figure S1).

Separate relaxation analyses were done for the $I^{CD2,inner}$, $I^{CD2,outer}$, and I^{CD3} integrated intensities from an array of $\tau_k \equiv \tau$ values. For most data sets, the plot of $\ln[I(\tau)]$ vs τ fit well to a straight line, and $R_2 \equiv$ best-fit slope. For the I^{CD2} data sets of GPfp and HAfp, pH 5, at 20 °C, the $\ln[I(\tau)]$ plot was nonlinear. These data fit well to a sum of two rate processes, i.e. $I(\tau) = [A_f \times \exp(-R_{2,f} \times \tau)] + [A_s \times \exp(-R_{2,s} \times \tau)]$ with f ≡ fast, s ≡ slow, $R_{2,f}$ and $R_{2,s}$ as rates, and A_f and A_s as the ratio of contributions to the signal intensity when $\tau = 0$ with $A_f + A_s = 1$.

RESULTS

Figure 3 displays DMPC-d54 spectra as a function of τ for some temperatures, and Figure S1 displays spectra for the shortest τ for all temperatures. The preparation of a sample, and the NMR data acquisition for the sample were typically done within the same month-long time period. Figure 3A

https://doi.org/10.1021/acs.biochem.1c00316
Biochemistry 2021, 60, 2637−2651

Table 1. ^{2}H NMR Transverse Relaxation Rates of DMPC-d54 (s^{-1})[a]

	peptide							
T (°C)	no peptide		GPfp		HAfp pH 7		HAfp pH 5	
	$-C^2H_2$	$-C^2H_3$	$-C^2H_2$	$-C^2H_3$	$-C^2H_2$	$-C^2H_3$	$-C^2H_2$	$-C^2H_3$
35	951(6)	313(9)	1147(7)	392(5)	1290(15)	477(13)	1110(11)	407(8)
30	950(9)	334(8)	1096(10)	407(4)	1518(35)	512(34)	1255(12)	413(12)
25	1078(23)	316(9)	1025(20)	418(4)	2116(53)	609(25)	1864(27)	516(8)
20	1878(33)	1009(15)	$R_{2,f}$ = 9480(918) s^{-1} A_f = 0.660(16) $R_{2,s}$ = 1782(59) s^{-1} A_s = 0.340(19)	928(32)	1935(40)	1177(29)	$R_{2,f}$ = 14088(374) s^{-1} A_f = 0.965(17) $R_{2,s}$ = 876(163) s^{-1} A_s = 0.035(4)	2745(92)
10	2136(22)	1194(20)	7030(127)	2980(80)	2068(15)	1085(26)	4347(131)	2505(106)
0	2994(64)	1548(25)	4078(141)	1736(68)	2772(64)	1710(28)	4286(118)	1409(42)

[a]Samples are DMPC-d54 without peptide or with peptide at a peptide:DMPC-d54 = 1:25 molar ratio. A relaxation rate is derived from fitting of integrated intensities (I) vs relaxation time (τ). For $-C^2H_2$, the intensities are sums for symmetric frequency ranges around 0 kHz, with typical values of (15 → 25) + (−15 → −25) kHz. For $-C^2H_3$, the intensities are the difference between integration over the central spectral region with $-C^2H_3$ and $-C^2H_2$ contributions and integration over nearby ranges that only contain $-C^2H_2$ contributions, with typical integration frequency ranges of (5 → −5) − [(10 → 15) + (−10 → −15)] kHz. The $-C^2H_2$ rates are typically for the most intense region of the $-C^2H_2$ spectrum that does not overlap with the $-C^2H_3$ signals. Figure S1 lists the frequency ranges for each fitting as well as fittings for other ranges and displays spectra at smallest τ. For most data, the R_2 relaxation rate was determined from fitting of ln (I) = ln (I_0) − ($R_2 \times \tau$) where ln (I_0) and R_2 are fitting parameters. For the $-C^2H_2$ GPfp and HAfp, pH 5, data at 20 °C, the fitting was based $I = [A_f \times \exp(-R_{2,f} \times \tau)] + [A_s \times \exp(-R_{2,s} \times \tau)]$ with f ≡ fast, s ≡ slow, and $R_{2,f}$, $R_{2,s}$, A_f, and A_s as fitting parameters with $A_f + A_s = 1$. Each best-fit parameter is followed by the fitting uncertainty in parentheses.

displays spectra of the four samples at 35 °C. The DMPC-d54 is in the liquid-crystalline phase, as evidenced by the maximal spectral width <40 kHz and the sharp symmetric pairs of "horns" that correspond to θ = 90° signals from the $-C^2H_3$ or specific $-C_n{}^2H_2$ groups along the myristoyl chains, with n = 2, 3, ... 13 (headgroup to methyl group). The individual DMPC-d54 molecules are rotating rapidly about the bilayer normal direction, and θ approximately corresponds to the angle between the local bilayer normal and the NMR field direction. The most prominent pair of horns with smallest frequency separation $\Delta\nu$ are assigned to the $-C^2H_3$ group (n = 14), and pairs with increasing $\Delta\nu$ are assigned to $-C_n{}^2H_2$ with monotonically decreasing n, with the outermost pair assigned to n = 2 → 6.[27] Overall, there are narrower spectra and smaller order parameters for the GPfp and HAfp, pH 5, vs no peptide and HAfp, pH 7, samples.

The intensities of the Figure 3A 35 °C spectra of the four samples exhibit similar decays with increasing τ, which supports similar R_2 values for all samples. There is also slower decay with increasing τ of the central vs outer spectral regions that respectively contain $-C^2H_3$ + $-C^2H_2$ vs only $-C^2H_2$ signals. These visual observations are borne out in the fittings of ln[$I(\tau)$] vs τ, with similar $R_2{}^{CD3}$'s of the four samples, similar $R_2{}^{CD2}$'s of the four samples, and $R_2{}^{CD2}/R_2{}^{CD3}$ ratios in the 2.7−3.0 range (Table 1 and Figure S1). For a particular sample, the $R_2{}^{CD2}$'s are similar for integrations in the outer and inner $-C^2H_2$ horn regions, where the former is dominated by $-C^2H_2$ closer to the headgroup and the latter has significant contributions from $-C^2H_2$ close to the methyl group (Figure S1). The Discussion section provides a more detailed description of the R_2's for the different samples and integration ranges. For HAfp, pH 7, there are similar R_2's determined from NMR data from a different sample with peptide:lipid = 1:50 (Figure S2). There was higher signal-to-noise for this sample so that $R_2{}^{CD2}$ was also determined from integration in the outermost region of the spectra that is dominated by θ close to 0°, i.e., a local bilayer normal parallel to the NMR field. The $R_2{}^{CD2}$ (0°)/$R_2{}^{CD2}$ (90°) ≈ 1.5 may reflect larger variations in the quadrupolar frequency for 0 vs 90° for equivalent amplitude acyl chain motion because of the $(3\cos^2\theta - 1)$ dependence of this frequency.

The trends observed for the 35 °C spectra are also generally observed for the 30 and 25 °C spectra, including $R_2{}^{CD2}/R_2{}^{CD3}$ ≈ 2.4−3.6 and similar values of $R_2{}^{CD2}$ for $-C^2H_2$ either closer to the headgroup or closer to the methyl group (Table 1 and Figure S1). At 25 °C, the no peptide and HAfp, pH 7, spectra have a broader background signal that is likely a gel phase, but this signal is subtracted during calculation of $I(\tau)$ and the reported R_2's are for the liquid-crystalline phase in the most intense region (∼20 → −20 kHz).

Relative to 25 °C, the no peptide and HAfp, pH 7 spectra are broader at 20 °C and consistent with a gel phase for which the acyl chains are much more ordered than the liquid-crystalline phase (Figures 3B,C and S1). There is additional broadening when the temperature is reduced to 10 and then 0 °C, which correlates with increased ordering (Figures 3D and S1). At 20 °C, the GPfp and HAfp, pH 5, spectra have some of the horn features of the liquid-crystalline phase, and their lineshapes and linewidths are intermediate between those of the 25 and 20 °C spectra of no peptide and HAfp, pH 7 (Figure 3B). At 10 °C, the GPfp and HAfp, pH 5, spectra are broader and no longer have horn features and at 0 °C are even broader and resemble the no peptide and HAfp, pH 7, spectra at 10 or 20 °C (Figure 3C,D).

Figure 3 displays the effect of increasing τ on spectral intensity, and each panel shows comparison between samples with similar spectral lineshapes and linewidths that reflect similar amplitudes of fast-motion of the acyl chains. Figure 3A displays the 35 °C data, as discussed above, and Figure 3B displays the 25 °C data for no peptide and HAfp, pH 7, and 20 °C data for GPfp and HAfp, pH 5. Visual comparison is straightforward between the no peptide and GPfp spectra in Figure 3B, because they were acquired with the same array of τ values. There is much more rapid decay of the intensities of the GPfp vs no peptide spectra. There is even more striking difference between the very rapid decay for HAfp, pH 5, vs the

https://doi.org/10.1021/acs.biochem.1c00316
Biochemistry 2021, 60, 2637−2651

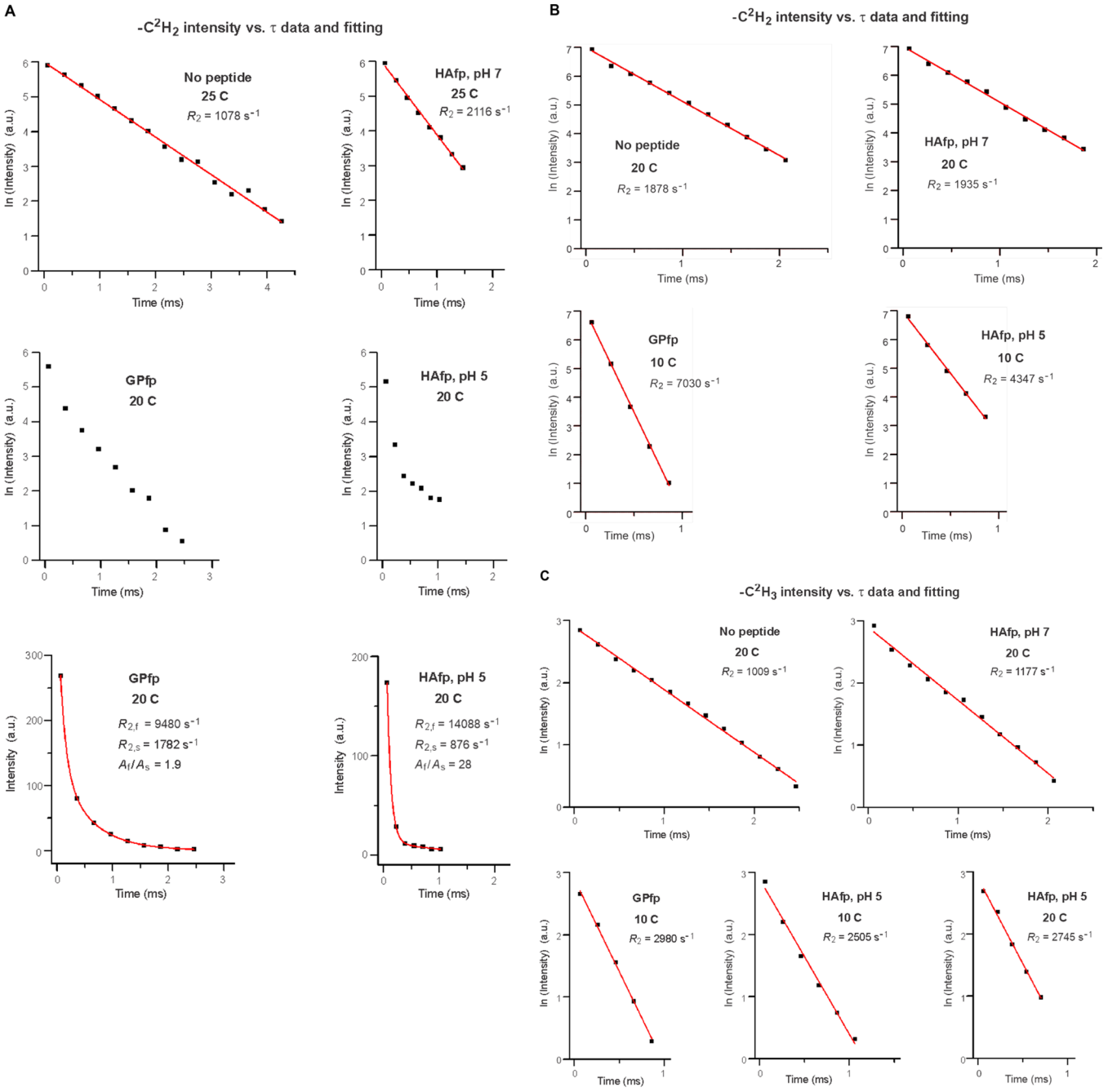

Figure 4. Fittings of ^{2}H NMR spectral intensity (I) vs relaxation time (τ) to determine R_2's ≡ transverse relaxation rates. Plots and fittings are for: (A) $-C_2H_2$ data of no peptide and HAfp, pH 7, at 25 °C and of GPfp and HAfp, pH 5, at 20 °C; (B) $-C_2H_2$ data of no peptide and HAfp, pH 7, at 20 °C and of GPfp and HAfp, pH 5, at 10 °C; and (C) $-C_2H_3$ data. The data are black squares and are based on integrated intensities from spectra displayed in (A) Figure 3B; (B) Figure 3C; and (C) Figure 3B,C. The best-fits are displayed in red. The fittings in panels A and B are grouped together because of similar lineshapes and linewidths of the respective Figure 3B,C spectra. Most data are fitted to $\ln(I) = \ln(I_0) - (R_2 \times \tau)$ where $\ln(I_0)$ and R_2 ≡ transverse relaxation rate are fitting parameters. For the GPfp and HAfp, pH 5 $-C^2H_2$ data at 20 °C, the fitting is based on $I = [A_f \times \exp(-R_{2,f} \times \tau)] + [A_s \times \exp(-R_{2,s} \times \tau)]$ where A_f, $R_{2,f}$, A_s, and $R_{2,s}$ are fitting parameters. Best-fit parameters with uncertainties are also displayed in Table 1, and Figure S1 has the integration windows that were used to determine the intensities that are fitted.

much slower decay for HAfp, pH 7 (note that the $\Delta\tau$ is smaller for HAfp, pH 5 vs 7). Figure 3C displays 20 °C data for no peptide and HAfp, pH 7, and 10 °C data for GPfp and HAfp, pH 5. Direct comparison can be made between all spectra, because they were acquired with the same array of τ values. There are similar slower decays of intensities of no peptide and HAfp, pH 7, vs more rapid decay of HAfp, pH 5, and even faster decay for GPfp. Similar trends are observed in Figure 3D, which displays comparative 10 °C data for no peptide and HAfp, pH 7, and 0 °C data for GPfp and HAfp, pH 5.

Figure 4A displays fittings of $-C^2H_2$ intensities measured from the Figure 3B spectra. For no peptide and HAfp, pH 7, at 25 °C, plots of $\ln[I^{CD2}]$ vs τ were linear, and R_2^{CD2} was the best-fit slope. For GPfp and HAfp, pH 5, at 20 °C, plots of $\ln[I^{CD2}]$ vs τ exhibited more rapid decay and were nonlinear, and I^{CD2} vs τ was fitted to a sum of fast and slow exponential

https://doi.org/10.1021/acs.biochem.1c00316
Biochemistry 2021, 60, 2637−2651

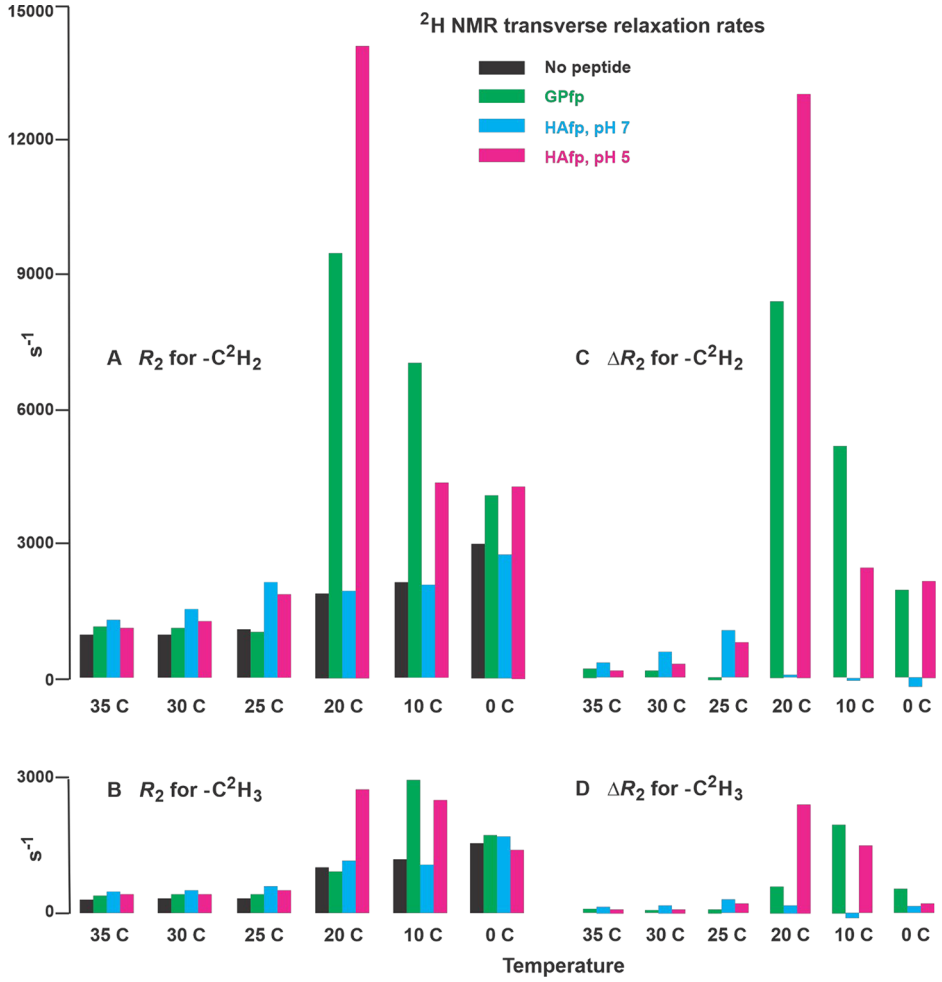

Figure 5. Bar plots of temperature-dependent transverse relaxation rates (R_2) and differences in rates (ΔR_2). Panels A and B display R_2's for $-C^2H_2$ and $-C^2H_3$, respectively, and panels C and D display ΔR_2's for $-C^2H_2$ and $-C^2H_3$, respectively, where $\Delta R_2 = R_{2,\text{peptide}} - R_{2,\text{no peptide}}$. The R_2's are for DMPC-d54 without peptide and with a peptide:DMPC-d54 molar ratio = 1:25. The R_2 values and their uncertainties are numerically presented in Table 1 with additional rate analyses in Figures S1 and S2. The $-C^2H_2$ R_2's are typically for the most intense region of the $-C^2H_2$ spectrum that does not overlap with the $-C^2H_3$ signals. For $-C^2H_2$ of GPfp and HAfp, pH 5, at 20 °C, the R_2's are for the dominant fast components of the biexponential decays. At 35, 30, and 25 °C, each ΔR_2 is calculated using $R_{2,\text{peptide}}$ and $R_{2,\text{no peptide}}$ at the given temperature, based on the predominant liquid-crystalline phase at these temperatures. At 20, 10, and 0 °C, each ΔR_2 for HAfp, pH 7, is also the difference between R_2's at the given temperature, based on a predominant gel phase and on similar spectral lineshapes and linewidths at each temperature (Figures 3C,D and S1). At 20, 10, and 0 °C, each ΔR_2 for GPfp and HAfp, pH 5, is calculated using the $R_{2,\text{no peptide}}$ at 25, 20, and 10 °C, respectively. This is based on similar spectral lineshapes and linewidths and therefore similar phases and amplitudes of fast-motions of the peptide and no peptide samples (Figure 3B–D).

decays. Figure 4B displays fittings of $\ln[I^{CD2}]$ vs τ based on the Figure 3C spectra, which show the more rapid decays and larger R_2^{CD2}'s of GPfp and HAfp, pH 5, vs no peptide and HAfp, pH 7. Figure 4C displays fittings of $\ln[I^{CD3}]$ vs τ based on the Figure 3B,C spectra. There are more rapid decays and larger R_2^{CD3}'s of GPfp and HAfp, pH 5, vs no peptide and HAfp, pH 7. The R_2^{CD2} and R_2^{CD3} values are presented numerically with uncertainties in Table 1 and displayed visually as bar plots in Figure 5A,B. The $-C^2H_2$ rates are typically for the most intense region of the $-C^2H_2$ spectrum that does not overlap with the $-C^2H_3$ signals. Figure S1 displays spectra at the shortest τ as well as all integration regions and R_2 values for the four samples. Figure S2 displays spectra and R_2's from a second HAfp, pH 7, sample with peptide:lipid = 1:50. For a given temperature and functional group, the R_2's of the two samples typically agree within 15%.

Figure 5C,D displays bar plots of $\Delta R_2 = R_{2,\text{peptide}} - R_{2,\text{no peptide}}$ for the $-CD_2$ and $-CD_3$ groups. The $R_{2,\text{peptide}}$'s are for peptide:lipid = 1:25. At 35, 30, and 25 °C, each ΔR_2 is calculated using $R_{2,\text{peptide}}$ and $R_{2,\text{no peptide}}$ at the given temperature, based on the predominant liquid-crystalline phase at these temperatures. At 20, 10, and 0 °C, each ΔR_2 for HAfp, pH 7, is also the difference between R_2's at the given temperature, based on the predominant gel phase and on similar spectral lineshapes and linewidths at each temperature (Figures 3 and S1). At 20, 10, and 0 °C, each ΔR_2 for GPfp and HAfp, pH 5, is calculated using the $R_{2,\text{no peptide}}$ at 25, 20, and 10 °C, respectively. This is based on similar spectral lineshapes and linewidths and therefore similar phases and amplitudes of fast-motions of the peptide and no peptide samples (Figure 3).

DISCUSSION

1. Summary of Experimental Results Including Distinctive Temperature Dependence of R_2 of GPfp and HAfp, pH 5. The present study reports the ^{2}H NMR

https://doi.org/10.1021/acs.biochem.1c00316
Biochemistry 2021, 60, 2637−2651

transverse relaxation rates of the acyl chains of the DMPC-d54 membrane as functions of bound fp and temperature. At 35, 30, and 25 °C, the spectral lineshapes of all samples are consistent with membrane with a predominant liquid-crystalline phase. At 20, 10, and 0 °C, the lineshapes of the no peptide and HAfp, pH 7, are consistent with a gel phase, whereas at 20 °C, those of GPfp and HAfp, pH 5, are intermediate between the two phases and have some of the "horn" features of liquid-crystalline spectra. At 10 and 0 °C, the lineshapes resemble those of no peptide and HAfp, pH 7 at 20 °C. As shown in Figure 5C,D, $\Delta R_2 = R_{2,\text{peptide}} - R_{2,\text{no peptide}}$ is separated in three groups: (1) for all peptides in liquid-crystalline lipid (35, 30, and 25 °C), the typical $\Delta R_2 > 0$ and increases with lower temperature with values up to $\sim 10^3$ Hz for $-CD_2$ and $\sim 3 \times 10^2$ Hz for $-CD_3$; (2) for HAfp, pH 7, in a gel phase (20, 10, and 0 °C), $\Delta R_2 \approx 0$; and (3) for GPfp and HAfp, pH 5, at 20, 10, and 0 °C, $\Delta R_2 > 0$, and exhibits a large increase and then decrease as temperature is lowered with maximum $\Delta R_2 \approx 10^4$ Hz for $-CD_2$ and 2×10^3 Hz for $-CD_3$.

Earlier studies have shown that acyl chain ^{2}H's of pure DMPC and other lipids exhibit an increase and decrease in R_2 in a ∼5 °C interval near the liquid-crystalline to rippled-gel phase transition.[53,54] This was not observed in our no peptide data, probably because the temperature was changed in larger increments. Earlier studies of deuterated DMPC or other lipid + peptide/protein have typically shown a smaller peak in ^{2}H R_2 near the phase-transition temperature.[55−57] Examples of the peptide/protein include gramicidin, a bacterial ion channel, and lung surfactant proteins that function to reduce the surface tension at the air−water interface in lung alveoli. By contrast, for the present study, GPfp and HAfp, pH 5, exhibit large R_2's at 20, 10, and 0 °C with the highest value typically at 20 or 10 °C (Figure 5A,B). HAfp, pH 7, shows a small increase in R_2 in the 20 to 0 °C range, similar to no peptide. The GPfp sample was prepared at neutral pH, at which GPfp has been shown to induce vesicle fusion, whereas HAfp induces greater fusion at pH 5 vs 7.

2. $\Delta R_2 > 0$ in the Liquid-Crystalline Phase Is Consistent with a Longer Correlation Time with Peptide. For the liquid-crystalline phase, the larger ^{2}H R_2's with bound fp correlate with earlier observation at 35 °C of a ∼2× larger ^{31}P R_2 of membrane with bound GPfp.[58] The ^{2}H R_2 has contributions from the motional spectral densities (J) at 0, ω_0, and $2\omega_0$ frequencies, where ω_0 is 2π times the ^{2}H NMR Larmor frequency = 61 MHz.[22] The $J(\omega_0)$ and $J(2\omega_0)$ contributions are small based on previously reported ^{2}H NMR longitudinal relaxation rates (R_1's) of similar samples at 35 °C.[58] The R_1's are ∼100× smaller than the respective R_2's and are a reasonable estimate of the $J(\omega_0)$ and $J(2\omega_0)$ contributions to R_2.[22,23] A reasonable estimate of the major $J(0)$ contribution to R_2 for a specific type of motion is $\Delta M_2 \times \tau_c$, where ΔM_2 is the mean-squared amplitude of the NMR frequency fluctuations associated with the motion and $\tau_c \approx J(0)/2$ is the correlation time of the motion, e.g., for angular motion, the typical time to move 1 rad.[23,59] This R_2 estimate is valid for "fast-motion", for which $\Delta M_2 \times \tau_c^2 \ll 1$. For deuterated lipid acyl chains, the ^{2}H $\Delta M_2 \approx (4 \times 10^{10}\ \text{s}^{-2}) \times (1 - S^2)$, where S is the order parameter for the motion.[22] A smaller S correlates with larger-amplitude motion and therefore larger ΔM_2, i.e., greater fluctuations in NMR frequency experienced by the ^{2}H nuclei. This ΔM_2 estimation is based on large-jump motion, and for continuous small jumps, ΔM_2 may be smaller for a given order parameter.[59] For the temperature range of the present study, the literature values of τ_c for typical lipid chain motions are $<10^{-6}$ s so that the fast-motion condition is valid.[54,60]

For the liquid-crystalline phase, acyl chain fluctuations perpendicular to the bilayer normal have the largest τ_c and are likely the biggest contributor to $J(0)$ and R_2.[60] For liquid-crystalline DMPC-d54, the typical $S \approx 0.2$ for $-CD_2$ groups so that $\Delta M_2 \approx 4 \times 10^{10}\ \text{s}^{-2}$.[27] Our typical experimental $R_2 \approx 10^3$ Hz in this phase, so the calculated $\tau_c \approx 2 \times 10^{-8}\ \text{s}^{-1}$, which matches literature values of τ_c for chain fluctuations and supports these fluctuations as the dominant motion underlying R_2.[60] For any fp sample in this phase, the typical $\Delta R_2 > 0$ (Figure 5C,D). Relative to without peptide, there is a literature report of ∼3× larger τ_c with 6 mol % integral membrane peptide that probably reflects peptide-associated disruption of large-amplitude chain motion.[54] There is probably a similar increase in τ_c for fp samples, and this increase is likely the basis for the $\Delta R_2 > 0$. The typically larger ΔR_2 for HAfp vs GPfp may be due to smaller separation between HAfp monomers vs GPfp oligomers and consequent greater probability of close contact between lipid and peptide. This difference is described more quantitatively by comparison of the typical lipid diffusion distance $\equiv d_L$ vs average separation between peptides $\equiv d_{\text{HAfp}}$ or d_{GPfp}. The $d_L \approx 60$ Å based on $d_L \approx (4 \times D \times \tau_D)^{1/2}$ with a lateral diffusion constant $D \approx 10^8\ \text{Å}^2\ \text{s}^{-1}$ and diffusion time $\tau_D \approx 10^{-5}$ s, chosen to be short enough for spectral averaging.[61] For a vesicle with ∼100 nm diameter, the surface area $\approx 3 \times 10^6\ \text{Å}^2$, $N_{\text{lipid}} \approx 6 \times 10^4$, and $N_{\text{fp}} \approx 2 \times 10^3$. The $d_{\text{HAfp}} \approx 40$ Å and $d_{\text{GPfp}} \approx 120$ Å (based on ∼10 GPfp per oligomer) so that $d_L < d_{\text{HAfp}}$ and $d_L > d_{\text{GPfp}}$, i.e., more lipids will contact HAfp monomers vs GPfp oligomers.[21] For the HAfp, pH 7, sample at a 1:50 ratio, $d_{\text{HAfp}} \approx 55$ Å so that $d_L < d_{\text{HAfp}}$ still holds. This correlates with R_2's for the 1:50 sample that are more similar to 1:25 HAfp than 1:25 GPfp (Figures S1 and S2).

3. $\Delta R_2 \approx 0$ for HAfp, pH 7, in Gel Phases Is Consistent with a Shorter Correlation Time with Peptide. At 20 °C, the spectral lineshape of DMPC-d54 without peptide is much broader than at higher temperature and is consistent with transition to a $L_{\beta'}$ rippled-gel phase for which there is higher ordering of the acyl chains and a reduced lateral diffusion rate.[52] The R_2^{20C}/R_2^{25C} is ∼2 for $-C^2H_2$ and ∼3 for $-C^2H_3$. There is greater spectral broadening at 10 °C and only a small increase in R_2's, with an R_2^{10C}/R_2^{20C} of ∼1.1. There is further broadening at 0 °C, consistent with the transition to the L_β phase for which the chains are fully ordered in a *trans* conformation. There is also an increase in R_2's, with $R_2^{0C}/R_2^{10C} \approx 1.4$. The increases in R_2 are semiquantitatively understood by the countervailing changes in ΔM_2 and τ_c. For the gel phases, a typical $S^{CD2} \approx 0.7$ so that $\Delta M_2 \approx 2 \times 10^{10}\ \text{s}^{-2}$, with increases in S and decreases in ΔM_2 as temperature is lowered.[22] The effect on R_2 of a ∼2× smaller ΔM_2 in a gel vs liquid-crystalline phase is more-than-compensated by increases in τ_c, including ∼5 and ∼3× increases with transitions to rippled-gel and gel phases, respectively.[60]

At 20, 10, and 0 °C, the spectral lineshapes with HAfp, pH 7, are similar to those of no peptide at the same temperature and consistent with gel phases. Interestingly, for HAfp, pH 7, $R_2^{20C} \approx R_2^{25C}$ and $\Delta R_2 \approx 0$ at 20, 10, and 0 °C (Figure 5). These observations are semiquantitatively explained if HAfp, pH 7, follows an earlier result for a transmembrane peptide of ∼2× smaller τ_c with vs without peptide in gel phases that likely reflects peptide disruption of chain ordering.[54] This behavior

https://doi.org/10.1021/acs.biochem.1c00316
Biochemistry 2021, 60, 2637−2651

contrasts with the earlier-described ~3× larger τ_c with peptide in the liquid-crystalline phase.

4. Very Large $\Delta R_2 \approx 10^4$ Hz for GPfp and HAfp, pH 5, at 20 °C Is Consistent with Larger-Amplitude Motion for Lipid Closer to vs Further from Peptide. In our view, the most interesting experimental result of our study is the large R_2's for GPfp and HAfp, pH 5, over the 20−0 °C range with a maximum $\Delta R_2^{CD2} \approx 10^4$ Hz at 20 °C and maximum $\Delta R_2^{CD3} \approx 2 \times 10^3$ Hz at 20 or 10 °C (Figure 5C,D). The large increases and then decreases in R_2's as temperature is lowered through the phase transitions are not explainable with only consideration of monotonic increases in τ_c as temperature is lowered. We provide a more quantitative interpretation of the R_2 behavior based on a model for the large ^{2}H R_2's near the phase separation temperature of lipid mixtures as well as the results of several molecular dynamics simulations. For the mixtures, lateral lipid diffusion between nm-size domains with different acyl chain order parameters is the proposed motion that results in large R_2's in these samples.[25,62] The ΔM_2 for this motion is approximately the difference in mean-squared NMR frequency fluctuations between the different domains, and the τ_c is the characteristic time for a lipid to diffuse between the domains. The same model is applied to the present study and the "domains" are lipids closer to vs more distant from the peptide. There is ~6 Å dimension of the peptide-proximal domain, which is much smaller than the ~20−200 Å dimension of the lipid domains of the earlier study.

Molecular dynamics simulations from multiple groups have shown significantly larger acyl chain motion for lipids close to (<6 Å) vs more distant from monomeric HAfp, with $-CD_2$ $S^{closer} \approx 0.1$ vs $S^{further} \approx 0.2$ in the liquid-crystalline phase.[47−49] The larger motion results in higher probability of protrusion of acyl chains into the aqueous phase for lipids close to HAfp, which may be relevant for reducing barriers between membrane fusion intermediates (Figure 1F). There is a $\Delta M_2 \approx (4 \times 10^{10}\ s^{-2}) \times (S^{2,further} - S^{2,closer}) \approx 10^9\ s^{-2}$ and the diffusion $\tau_D \approx \tau_c \approx (6\ Å)^2/4D$ with $D \approx 10^8$ Å^2/s so that $\tau_c \approx 10^{-7}$ s, and the calculated $\Delta R_2^{CD2} \approx \Delta M_2 \times \tau_c \approx 10^2$ Hz. This could contribute to the experimental ΔR_2^{CD2} of GPfp and HAfp, pH 5, which is typically in the range of $2-8 \times 10^2$ Hz in the 35−25 °C temperature range.

We propose that this phenomenon also exists at 20 °C and is the basis for the large ΔR_2's. The lineshapes for GPfp and HAfp, pH 5, are intermediate between those of liquid-crystalline and rippled-gel phases, and we estimate $S^{closer} \approx 0.2$ vs $S^{further} \approx 0.5$ so that $\Delta M_2 \approx 10^{10}\ s^{-2}$. The $D \approx 10^7$ Å^2/s so that for a 6 Å diffusion length, $\tau_c \approx 10^{-6}$ s and $\Delta R_2^{CD2} \approx 10^4$ Hz, which is in semiquantitative agreement with the experimental ΔR_2's.[61] Because $1/\tau_c <$ spectral width, there is spectral averaging between the two lipid locations and S values, which is consistent with the observed single lineshapes at 20 °C.

At 10 °C, the experimental ΔR_2^{CD2}'s are smaller than at 20 °C but still substantial (up to 5×10^3 Hz). The lateral diffusion τ_c is larger at 10 °C, so within the present model, the ΔM_2 would have to be smaller at 10 vs 20 °C. There are similar lineshapes and linewidths of the spectra of the 10 °C peptide and the 20 °C no peptide samples, where the latter is in the rippled-gel phase, which has larger domains of lipids with more- and less-ordered acyl chains.[52] If the 10 °C peptide sample also adopts this phase, these larger domains may diminish the distinction between lipids closer to vs further from the peptide so that ΔM_2 is reduced. At 0 °C, the experimental $\Delta R_2^{CD2} \approx 10^3$ Hz, which is a continuation of the trend of a smaller ΔR_2 with temperature reduction in the gel phases.

5. Similar Trends and Smaller ΔR_2 for $-CD_3$ vs $-CD_2$ Support Scaling of ΔM_2 and the Diffusion Model. The ΔR_2^{CD3}'s of the peptide samples follow the same trends as the ΔR_2^{CD2}'s but with smaller values. The ΔR_2^{CD3}'s increase as temperature is lowered in the liquid-crystalline phase with the largest $\Delta R_2^{CD3} \approx 3 \times 10^2$ Hz at 25 °C. For a peptide sample at a given temperature, the typical $\Delta R_2^{CD3}/\Delta R_2^{CD2} \approx 1/3$, which matches the no peptide $R_2^{CD3}/R_2^{CD2} \approx 1/3$ and is a likely consequence of scaling down of the relevant ΔM_2 for acyl chain fluctuations for $-CD_3$ by rapid rotation about the symmetry axis. For GPfp and HAfp, pH 5, the $-CD_3$ ΔR_2 also exhibits the increase-then-decrease trend as temperature is further lowered and the lipid adopts gel phases. The maximum $\Delta R_2^{CD3} \approx 2 \times 10^3$ Hz is ~1/5 of the maximum ΔR_2^{CD2}. For GPfp, the largest ΔR_2 is at 10 vs 20 °C for $-CD_3$ vs $-CD_2$. The $-CD_3$ and $-CD_2$ should experience the same lateral diffusion τ_c, but the $-CD_3$ has a much smaller order parameter so that lower temperature may be needed for an appreciable difference in $(1 - S^2)$ and ΔM_2 for a lipid closer to vs further from peptide.

6. Much Larger ΔR_2 for β Sheet GPfp and Helical Hairpin HAfp, pH 5, Correlates with Greater Hydrophobicity and Fusion. For HAfp, pH 7, at 20, 10, and 0 °C, the $\Delta R_2 \approx 0$ for $-CD_2$ and $-CD_3$ groups, which is very different from GPfp and HAfp, pH 5. HAfp, pH 7, also exhibits spectral lineshapes and order parameters that are comparable to or a little broader/larger than no peptide, whereas GPfp and HAfp, pH 5, exhibit lineshapes and order parameters that are smaller than no peptide and HAfp, pH 7 (Figure 3). Earlier NMR shows that HAfp is mixture of different helical hairpin structures at pH 5 and 7 (Figure 2B). At pH 5, NMR data support a greater fraction of more open/"semiclosed" structure that has a greater hydrophobic surface area that may be a better solvent for lipid acyl chains and allow greater probability for lipid acyl chain location outside the hydrophobic core of the membrane (Figure 1F).[18] By contrast, at pH 7, HAfp has a smaller hydrophobic surface area, and the chain motion may be similar for lipids closer to vs further from HAfp, which is consistent with pH 7 order parameters similar to pure lipid.[27] This similarity would result in $\Delta M_2 \approx 0$ for diffusion, like pure lipid, so that $\Delta R_2 \approx 0$.

There is correlation between the small effects on the lipid ^{2}H NMR lineshape and R_2 of HAfp at pH 7 vs much larger effects at pH 5 and the difference in the appearance of a vesicle suspension after addition of HAfp at pH 7 vs 5. The vesicles are ~100 nm in diameter, and the suspension at either pH 7 or 5 is transparent prior to addition. After HAfp addition at pH 7, the suspension remains transparent. By contrast, addition at pH 5 results in a cloudy/turbid suspension that is the likely result of HAfp-induced vesicle fusion and consequent larger vesicles, with increased light scattering when the vesicle dimension is greater than ~300 nm.[63] This observation is consistent with pH dependence of vesicle fusion by fluorescence measurement and with large pH dependence of hemolysis of erythrocytes after addition of HAfp.[18,64] Cloudiness/turbidity is also apparent in vesicle suspensions after addition of GPfp, and electron micrographs from earlier studies also show larger dimension vesicles after addition of GPfp.[38,65,66] There is correlation between the large ΔR_2's for GPfp and HAfp, pH 5, and their fusogenicity that we ascribe to

https://doi.org/10.1021/acs.biochem.1c00316
Biochemistry 2021, 60, 2637−2651

increased protrusion of lipid acyl chains into the aqueous phase. This protrusion matches the chain location for transition states between membrane fusion intermediates (Figure 1F).

The similar spectral lineshapes of the no peptide and HAfp, pH 7, samples raise the possibility that HAfp does not bind to lipid. However, there are also two lines of evidence that support near-quantitative binding of HAfp at pH 7 for our samples. First, among the peptides, HAfp, pH 7, exhibits the largest ΔR_2's in the liquid-crystalline phase (Figure 5C,D). Second, $A_{280} < 0.01$ in the supernatant after centrifugation of the suspension containing lipid and HAfp. This second observation is independently supported by calculated $[HAfp_{bound}]/[HAfp_{free}] \approx K_{eq} \times [lipid] \approx 50$, based on $K_{eq} \approx 1 \times 10^4$ M^{-1}, the previously reported binding constant of HAfp with lipid at pH 7, and $[lipid] \approx 5 \times 10^{-3}$ M during our sample preparation.[64]

There is also the possibility that the different lineshapes and ΔR_2's for HAfp, pH 7 vs 5, are a consequence of different HAfp locations in the membrane, e.g., interfacial vs deeply inserted or transmembrane. In our view, the membrane location(s) of HAfp remains an unresolved question. There are experimental data that support both interfacial and deep membrane location, and different molecular dynamics simulations also find different "equilibrium" locations that vary between interfacial and transmembrane.[15,44,47,48,67−69] These differences may be a consequence of different initial conditions for HAfp structure and location. To our knowledge, only small changes in membrane location have been observed at pH 5 vs 7.[39,40] We therefore think that the large pH dependence of lipid/HAfp interaction is more likely due to a change in HAfp structural distribution and hydrophobicity, as detailed above.

7. Slow-Relaxing Fraction at 20 °C May Be Lipids That Do Not Contact GPfp. Other than the $-CD_2$ signals of GPfp and HAfp, pH 5, at 20 °C, the other data are all well-fitted by a single-exponential decay and one R_2. This likely means that all analyzed nuclei experience the same motions that dominate R_2. These motions have the largest τ_c and an appreciable ΔM_2 with a contribution to $R_2 \approx \Delta M_2 \times \tau_c$. As discussed above, for pure lipid, the dominant motion is likely acyl chain fluctuations perpendicular to the bilayer normal. This is also the likely motion for all the peptide samples in liquid-crystalline phase at 35, 30, and 25 °C. There are similar R_2's for no peptide and HAfp, pH 7, in the gel phases at 20, 10, and 0 °C, which supports similar dominant motion for the two samples (Figure 5A,B). At a given temperature, there are also similar spectral lineshapes for these two samples.

Fitting with a sum of fast (f) and slow (s) exponential decays was done for $-CD_2$ analyses of GPfp and HAfp, pH 5, samples at 20 °C. Fitting parameters were populations A_f and A_s and rates $R_{2,f}$ and $R_{2,s}$. These $R_{2,f}$'s had the largest $\Delta R_2 \approx 10^4$ Hz of all fittings, and as discussed in #4 above, we ascribe the ΔR_2 to lipid lateral diffusion between locations closer to vs further from the peptide, with different order parameters for the two locations.

We first consider the GPfp analysis for which the fast:slow population ratio $A_f/A_s \approx 2$ and the $R_{2,s}$ is similar to the R_2 of no peptide and HAfp, pH 7, at 20 °C, i.e., $\Delta R_{2,s} \approx 0$. This suggests that the slow fraction is lipids that do not contact GPfp. This hypothesis is supported by considering the model from #2 above with a vesicle with ∼100 nm diameter, surface area $\approx 3 \times 10^6$ Å^2, $N_{lipid} \approx 6 \times 10^4$, and $N_{GPfp} \approx 2 \times 10^3$. For GPfp oligomers with ∼10 peptides and ∼16 residues in a β sheet structure, the area per oligomer is ∼(50 Å^2), and there is a ∼120 Å average distance between oligomers.[14] For a lateral diffusion constant $D \approx 10^7$ Å^2/s and a $\sim 10^{-5}$ s diffusion time consistent with spectral averaging, there is a ∼20 Å diffusion distance by a lipid. There is a difference of ∼30 Å between the oligomer separation (∼120 Å) and the sum of the oligomer and lipid diffusion dimensions (∼90 Å). This difference means there are regions of the vesicle containing lipids that do not contact GPfp during the diffusion time. Although our ΔR_2 model incorporates molecular dynamics results that show smaller order parameters for lipids closer to vs further from peptide, there are similar experimental lineshapes for the fast- and slow-relaxing lipid populations, which is consistent with fast-relaxing lipids spending relatively small fractional time next to a GPfp oligomer.

The above model is also applicable to the biexponential decay fitting of the HAfp, pH 5, data at 20 °C and explains the much smaller slow population for HAfp, pH 5 with $A_f/A_s \approx 28$. HAfp is monomeric, and the peptides are separated by ∼40 Å, which is approximately the lipid diffusion dimension. There are negligible regions of the vesicle with lipids that do not contact HAfp and have the associated $R_{2,s}$.

Unlike $-CD_2$, the $-CD_3$ data for GPfp at 20 °C are well-fitted by a single-exponential decay, and the R_2^{CD3} is intermediate between the R_2^{CD3}'s at 25 and 20 °C for either no peptide or HAfp, pH 7. As discussed above in #5, the $-CD_3$ and $-CD_2$ should experience the same diffusion τ_c, but the $-CD_3$ has a much smaller order parameter. At 20 °C, there may be a fairly small difference in $(1 - S^2)$ for $-CD_3$ for lipid closer to vs further from peptide so that ΔM_2^{CD3} and ΔR_2^{CD3} are smaller, which results in similar R_2^{CD3}'s for lipids that contact and do not contact GPfp. The $-CD_3$ data for HAfp, pH 5, at 20 °C are also well-fitted by a single-exponential decay, and the $\Delta R_2^{CD3} \approx 2 \times 10^3$ Hz. The lack of a second slower decay for $-CD_3$ is likely due to a combination of a small A_s, a smaller difference between $R_{2,f}$ and $R_{2,s}$, and smaller signals for $-CD_3$ vs $-CD_2$.

At 10 and 0 °C, the GPfp and HAfp, pH 5, $-CD_2$ and $-CD_3$ data are well-fitted as single-exponential decays, as evidenced by a typical $(\delta R_2/R_2) \approx 0.03$ where δR_2 is the fitting uncertainty. The typical $\Delta R_2 > 0$ but is significantly smaller than the $\sim 10^4$ Hz values for $-CD_2$ fitting of GPfp and HAfp, pH 5, data at 20 °C. We note that even for the $-CD_2$ GPfp data at 20 °C with $R_{2,f}/R_{2,s} \approx 5$, the Figure 4A $\ln(I^{CD2})$ vs time plot is reasonably linear, except for the point at shortest time. If there is a second slower decay in the 10 and 0 °C data, the $R_{2,f}/R_{2,s}$ ratio would be smaller than at 20 °C, and nonlinearity likely would not be apparent in the single decay fitting.

8. Lipid Ordering with fp with EPR and Fluorescence May Reflect fp−Lipid Label Interaction. The interpretation of the large ΔR_2 for GPfp and HAfp, pH 5, in terms of large-amplitude acyl chain motions is consistent with smaller average lipid order parameters relative to no peptide and HAfp, pH 7, from ^{2}H NMR spectra, X-ray scattering, and molecular dynamics simulations but not with larger-order parameters from EPR and fluorescence spectra.[19,27,41,47−50,70,71] These latter experiments share common features including membrane with a small fraction of lipid with an organic ring spin- or fluorescence-label at a particular site and measurement of the EPR lineshape or fluorescence anisotropy of the label. Increased anisotropy for the label for membrane with fp vs without fp is considered representative of increased order for

https://doi.org/10.1021/acs.biochem.1c00316
Biochemistry 2021, 60, 2637−2651

all membrane lipids. There may be a specific interaction of fusion peptide with the EPR and fluorescence label, which results in ordering of the label. This hypothesis is consistent with the observation that when [fusion peptide] ≈ [spin-labeled lipid], the ordering of the label is already close to its maximal value. By contrast, the simulation, NMR, and X-ray results were based on data that probe all of the lipids in the sample. For most of the above studies, the lipid was in the liquid-crystalline phase, and phosphatidylcholine was the major or only lipid headgroup, so the difference in disordering vs ordering between techniques is likely not due to lipid differences. In addition, the X-ray studies detected disordering with GPfp for a variety of lipid compositions that included a single phosphatidylcholine lipid with or without cholesterol as well a mixture that approximately matches the lipid composition of the plasma membrane of host cells of HIV. In most studies, lipid disordering or ordering was also correlated with fusion by comparison between different peptide:lipid ratios and/or comparison between wild-type and mutant peptide or between conditions that affect peptide-induced vesicle fusion, e.g., pH 5 vs 7 for HAfp.

We also note conflicting results between analyses of X-ray vs neutron scattering data about other effects on the membrane by GPfp. For both approaches, the GPfp had a significant fraction of an oligomeric β sheet structure. Analysis of the low-angle X-ray scattering showed a ∼3 Å thinner membrane width in the presence of GPfp, whereas analysis of small-angle neutron scattering showed a ∼3 Å thicker width.[50,72] Analysis of the X-ray data showed a typical 5−10-fold reduction in the bending modulus of membrane when GPfp was bound, whereas analysis of neutron spin−echo spectra showed a typical 1.6-fold increase in the bending modulus.[72,73] The X-ray vs neutron data are respectively consistent with membrane with larger vs smaller amplitudes of lipid motion. The reasons for these conflicting results are not understood, but we note there was some difference in the GPfp sequence used for the X-ray vs neutron experiments.

9. Detailed Fitting Gives Precise R_2^{CD3}, $R_2^{CD2,outer}$, and $R_2^{CD2,inner}$s, and $R_2^{outer} > R_2^{inner}$ Is Consistent with $\tau_c^{outer} > \tau_c^{inner}$ for Chain Fluctuations. For the present study, separate fittings are required for the I^{CD2} and I^{CD3} intensities, because (1) I^{CD2} is dominant at shorter times, based on 24 $-C^2H_2$ vs 6 $-C^2H_3$, and (2) I^{CD3} is dominant at longer times, based on $R_2^{CD3} < R_2^{CD2}$ (Figure 3). The spectral integrations include $I^{central}$ from the central region that has both $-C^2H_2$ and $-C^2H_3$ contributions and I^{outer} and I^{inner} from outlying regions that are only $-C^2H_2$ (Figure S1). Typically, I^{outer} is weighted toward $-C^2H_2$'s closer to the headgroup with a larger S, and I^{inner} is weighted toward $-C^2H_2$'s closer to the chain termini with smaller S. Each R_2^{CD3} is well-fitted using $I^{central} - I^{inner}$, with a typical $\delta R_2^{CD3}/R_2^{CD3} \approx 0.02$ (Table 1 and Figure 4C).

The $-CD_2$ R_2^{outer} and R_2^{inner} are determined from separate fittings of I^{outer} and I^{inner} (Figures S1 and S3). Between 35 and 10 °C, no peptide and HAfp, pH 7, exhibit a typical R_2^{outer}:$R_2^{inner} \approx 1.1$ and 1.2, respectively. As discussed above in #2, the $R_2 \approx \Delta M_2 \times \tau_c$ for these samples, and the $R_2^{outer} > R_2^{inner}$ is reasonably explained by $\tau_c^{outer} > \tau_c^{inner}$, which is consistent with lower mobility of $-C^2H_2$ closer to the headgroup vs chain termini. The larger R_2^{outer}:R_2^{inner} for HAfp, pH 7, vs no peptide could be due to HAfp location near the headgroups. At 0 °C, there is significant broadening of the $-C^2H_3$ contribution so that the inner and outer $-C^2H_2$ ranges are moved to regions corresponding to $-C^2H$ bond orientations respectively closer to perpendicular and parallel to the external magnetic field direction. This may be related to $R_2^{inner} > R_2^{outer}$ at 0 °C, with ratio of ∼1.1. Interestingly, the GPfp and HAfp, pH 5, typically have similar R_2^{outer} and R_2^{inner} at a given temperature but do not exhibit clear trends like no peptide and HAfp, pH 7 (Figure S3). For $-C^2H_2$'s nearer the headgroup vs chain termini, there may be different temperature dependences of S^{closer} and $S^{further}$, which results in different temperature dependences of ΔR_2^{outer} and ΔR_2^{inner}.

SUMMARY

In this study, ^{2}H NMR R_2's were determined for DMPC-d54 with bound GPfp and HAfp fusion peptides that adopt very different structures, an intermolecular antiparallel β sheet and monomer helical hairpin, respectively. For the liquid-crystalline phase between 35 and 25 °C, the typical $R_{2,peptide} > R_{2,no\ peptide}$, which is consistent with a larger correlation time τ_c for acyl chain fluctuations with peptide. For no peptide in the gel phase at 20 °C, the R_2's are ∼2× times larger than in the liquid-crystalline phase, and there is a ∼1.5× further increase when temperature is reduced to 0 °C, which correlates with increases in τ_c in the gel phases. At 20 °C, there are similar R_2's and spectral lineshapes for no peptide and HAfp, pH 7, and also similar R_2's at 10 and 0 °C, which correlates with earlier observations of similar τ_c's without vs with peptide in gel phases. GPfp and HAfp, pH 5, exhibit very different R_2's and lineshapes at 20, 10, and 0 °C. The $\Delta R_2^{CD2} \approx 10^4$ Hz at 20 °C, with smaller but still substantial ΔR_2's at 10 and 0 °C. At a given temperature, the lineshapes are also narrower than those of no peptide and HAfp, pH 7. The large ΔR_2's for GPfp and HAfp, pH 5, are interpreted to be due to lipid diffusion between locations closer to vs further from peptide, with respective smaller vs larger order parameters. This difference in order parameters was previously detected in molecular dynamics simulations of membrane with HAfp. Larger-amplitude chain motion, including protrusion into the aqueous phase, is likely characteristic of transition states between membrane fusion intermediates, and such motion is supported by the present study as a contribution of fusion peptides to fusion catalysis. This contribution exists for both helical and β sheet fusion peptide structures.

ASSOCIATED CONTENT

Supporting Information

The Supporting Information is available free of charge at https://pubs.acs.org/doi/10.1021/acs.biochem.1c00316.

Spectra at shortest τ, integration regions, and R_2 values and uncertainties; bar graphs of $R_2^{CD2,outer}$ and $R_2^{CD2,inner}$ (PDF)

AUTHOR INFORMATION

Corresponding Author

David P. Weliky − *Department of Chemistry, Michigan State University, East Lansing, Michigan 48824, United States;* orcid.org/0000-0002-2765-5950; Phone: 517-353-1177; Email: weliky@chemistry.msu.edu

Author

Ujjayini Ghosh − *Department of Chemistry, Michigan State University, East Lansing, Michigan 48824, United States*

Complete contact information is available at: https://pubs.acs.org/10.1021/acs.biochem.1c00316

Notes

The authors declare no competing financial interest.
GP, UniProt KB, P04578; HA, UniProtKB P03377.

■ ACKNOWLEDGMENTS

This work was supported by the National Institutes of Health grant number R01 AI047153.

■ ABBREVIATIONS

d, distance; *D*, diffusion constant; DMPC-d54, dimyristoylphosphatidylcholine with perdeuterated acyl chains; DOPC, dioleoylphosphatidylcholine; DPPC-d62, dipalmitoylphosphatidylcholine with perdeuterated acyl chains; Ed, ectodomain; f, fast; fp, fusion peptide; FsSu, fusion subunit; GP, HIV glycoprotein; HA, influenza hemagglutinin; *I*, intensity; LUV, large unilamellar vesicle; M_2, spectral second moment; *n*, carbon number in acyl chain; R_1, NMR longitudinal relaxation rate; R_2, NMR transverse relaxation rate; RbSu, receptor-binding subunit; s, slow; *S*, order parameter; SARS-CoV-2, severe acute respiratory syndrome coronavirus 2; δ, uncertainty; ΔM_2, mean-squared amplitude of the NMR frequency fluctuations; θ, angle with respect to NMR field direction; ν, frequency; τ, NMR time delay; τ_c, correlation time; τ_D, diffusion time

■ REFERENCES

(1) White, J. M.; Delos, S. E.; Brecher, M.; Schornberg, K. Structures and mechanisms of viral membrane fusion proteins: Multiple variations on a common theme. *Crit. Rev. Biochem. Mol. Biol.* **2008**, *43*, 189−219.
(2) Boonstra, S.; Blijleven, J. S.; Roos, W. H.; Onck, P. R.; van der Giessen, E.; van Oijen, A. M. Hemagglutinin-mediated membrane fusion: A biophysical perspective. *Annu. Rev. Biophys.* **2018**, *47*, 153−173.
(3) Tang, T.; Bidon, M.; Jaimes, J. A.; Whittaker, G. R.; Daniel, S. Coronavirus membrane fusion mechanism offers a potential target for antiviral development. *Antiviral Res.* **2020**, *178*, 104792.
(4) Pabis, A.; Rawle, R. J.; Kasson, P. M. Influenza hemagglutinin drives viral entry via two sequential intramembrane mechanisms. *Proc. Natl. Acad. Sci. U. S. A.* **2020**, *117*, 7200−7207.
(5) Kim, C. S.; Epand, R. F.; Leikina, E.; Epand, R. M.; Chernomordik, L. V. The final conformation of the complete ectodomain of the HA2 subunit of Influenza Hemagglutinin can by itself drive low pH-dependent fusion. *J. Biol. Chem.* **2011**, *286*, 13226−13234.
(6) Durrer, P.; Galli, C.; Hoenke, S.; Corti, C.; Gluck, R.; Vorherr, T.; Brunner, J. H+-induced membrane insertion of influenza virus hemagglutinin involves the HA2 amino-terminal fusion peptide but not the coiled coil region. *J. Biol. Chem.* **1996**, *271*, 13417−13421.
(7) Nobusawa, E.; Aoyama, T.; Kato, H.; Suzuki, Y.; Tateno, Y.; Nakajima, K. Comparison of complete amino acid sequences and receptor binding properties among 13 serotypes of hemagglutinins of influenza A viruses. *Virology* **1991**, *182*, 475−485.
(8) Freed, E. O.; Delwart, E. L.; Buchschacher, G. L., Jr.; Panganiban, A. T. A mutation in the human immunodeficiency virus type 1 transmembrane glycoprotein gp41 dominantly interferes with fusion and infectivity. *Proc. Natl. Acad. Sci. U. S. A.* **1992**, *89*, 70−74.
(9) Durell, S. R.; Martin, I.; Ruysschaert, J. M.; Shai, Y.; Blumenthal, R. What studies of fusion peptides tell us about viral envelope glycoprotein-mediated membrane fusion. *Mol. Membr. Biol.* **1997**, *14*, 97−112.
(10) Qiao, H.; Armstrong, R. T.; Melikyan, G. B.; Cohen, F. S.; White, J. M. A specific point mutant at position 1 of the influenza hemagglutinin fusion peptide displays a hemifusion phenotype. *Mol. Biol. Cell* **1999**, *10*, 2759−2769.
(11) Jaroniec, C. P.; Kaufman, J. D.; Stahl, S. J.; Viard, M.; Blumenthal, R.; Wingfield, P. T.; Bax, A. Structure and dynamics of micelle-associated human immunodeficiency virus gp41 fusion domain. *Biochemistry* **2005**, *44*, 16167−16180.
(12) Qiang, W.; Bodner, M. L.; Weliky, D. P. Solid-state NMR spectroscopy of human immunodeficiency virus fusion peptides associated with host-cell-like membranes: 2D correlation spectra and distance measurements support a fully extended conformation and models for specific antiparallel strand registries. *J. Am. Chem. Soc.* **2008**, *130*, 5459−5471.
(13) Madu, I. G.; Roth, S. L.; Belouzard, S.; Whittaker, G. R. Characterization of a highly conserved domain within the Severe Acute Respiratory Syndrome coronavirus spike protein S2 domain with characteristics of a viral fusion peptide. *J. Virol.* **2009**, *83*, 7411−7421.
(14) Schmick, S. D.; Weliky, D. P. Major antiparallel and minor parallel beta sheet populations detected in the membrane-associated Human Immunodeficiency Virus fusion peptide. *Biochemistry* **2010**, *49*, 10623−10635.
(15) Lorieau, J. L.; Louis, J. M.; Bax, A. The complete influenza hemagglutinin fusion domain adopts a tight helical hairpin arrangement at the lipid:water interface. *Proc. Natl. Acad. Sci. U. S. A.* **2010**, *107*, 11341−11346.
(16) Sackett, K.; Nethercott, M. J.; Zheng, Z. X.; Weliky, D. P. Solid-state NMR spectroscopy of the HIV gp41 membrane fusion protein supports intermolecular antiparallel beta sheet fusion peptide structure in the final six-helix bundle state. *J. Mol. Biol.* **2014**, *426*, 1077−1094.
(17) Ratnayake, P. U.; Sackett, K.; Nethercott, M. J.; Weliky, D. P. pH-dependent vesicle fusion induced by the ectodomain of the human immunodeficiency virus membrane fusion protein gp41: Two kinetically distinct processes and fully-membrane-associated gp41 with predominant beta sheet fusion peptide conformation. *Biochim. Biophys. Acta, Biomembr.* **2015**, *1848*, 289−298.
(18) Ghosh, U.; Xie, L.; Jia, L. H.; Liang, S.; Weliky, D. P. Closed and semiclosed interhelical structures in membrane vs closed and open structures in detergent for the Influenza Virus hemagglutinin fusion peptide and correlation of hydrophobic surface area with fusion catalysis. *J. Am. Chem. Soc.* **2015**, *137*, 7548−7551.
(19) Lai, A. L.; Millet, J. K.; Daniel, S.; Freed, J. H.; Whittaker, G. R. The SARS-CoV fusion peptide forms an extended bipartite fusion platform that perturbs membrane order in a calcium-dependent manner. *J. Mol. Biol.* **2017**, *429*, 3875−3892.
(20) Ranaweera, A.; Ratnayake, P. U.; Weliky, D. P. The stabilities of the soluble ectodomain and fusion peptide hairpins of the Influenza virus hemagglutinin subunit II protein are positively correlated with membrane fusion. *Biochemistry* **2018**, *57*, 5480−5493.
(21) Bodner, M. L.; Gabrys, C. M.; Parkanzky, P. D.; Yang, J.; Duskin, C. A.; Weliky, D. P. Temperature dependence and resonance assignment of ^{13}C NMR spectra of selectively and uniformly labeled fusion peptides associated with membranes. *Magn. Reson. Chem.* **2004**, *42*, 187−194.
(22) Davis, J. H. Deuterium magnetic resonance study of the gel and liquid crystalline phases of dipalmitoyl phosphatidylcholine. *Biophys. J.* **1979**, *27*, 339−358.
(23) Harris, R. K. *Nuclear magnetic resonance spectroscopy: A physiochemical view*; Longman, 1986.
(24) Rozovsky, S.; McDermott, A. E. The time scale of the catalytic loop motion in triosephosphate isomerase. *J. Mol. Biol.* **2001**, *310*, 259−270.
(25) Veatch, S. L.; Soubias, O.; Keller, S. L.; Gawrisch, K. Critical fluctuations in domain-forming lipid mixtures. *Proc. Natl. Acad. Sci. U. S. A.* **2007**, *104*, 17650−17655.
(26) Bloom, M.; Evans, E.; Mouritsen, O. G. Physical properties of the fluid lipid-bilayer component of cell membranes: a perspective. *Q. Rev. Biophys.* **1991**, *24*, 293−397.
(27) Ghosh, U.; Weliky, D. P. ^{2}H nuclear magnetic resonance spectroscopy supports larger amplitude fast motion and interference with lipid chain ordering for membrane that contains beta sheet

https://doi.org/10.1021/acs.biochem.1c00316
Biochemistry 2021, 60, 2637−2651

human immunodeficiency virus gp41 fusion peptide or helical hairpin influenza virus hemagglutinin fusion peptide at fusogenic pH. *Biochim. Biophys. Acta, Biomembr.* **2020**, *1862*, 183404.
(28) Wasniewski, C. M.; Parkanzky, P. D.; Bodner, M. L.; Weliky, D. P. Solid-state nuclear magnetic resonance studies of HIV and influenza fusion peptide orientations in membrane bilayers using stacked glass plate samples. *Chem. Phys. Lipids* **2004**, *132*, 89−100.
(29) Gabrys, C. M.; Weliky, D. P. Chemical shift assignment and structural plasticity of a HIV fusion peptide derivative in dodecylphosphocholine micelles. *Biochim. Biophys. Acta, Biomembr.* **2007**, *1768*, 3225−3234.
(30) Li, Y. L.; Tamm, L. K. Structure and plasticity of the human immunodeficiency virus gp41 fusion domain in lipid micelles and bilayers. *Biophys. J.* **2007**, *93*, 876−885.
(31) Lakomek, N. A.; Kaufman, J. D.; Stahl, S. J.; Louis, J. M.; Grishaev, A.; Wingfield, P. T.; Bax, A. Internal dynamics of the homotrimeric HIV-1 viral coat protein gp41 on multiple time scales. *Angew. Chem., Int. Ed.* **2013**, *52*, 3911−3915.
(32) Curtis-Fisk, J.; Spencer, R. M.; Weliky, D. P. Native conformation at specific residues in recombinant inclusion body protein in whole cells determined with solid-state NMR spectroscopy. *J. Am. Chem. Soc.* **2008**, *130*, 12568−12569.
(33) Sun, Y.; Weliky, D. P. ^{13}C-^{13}C Correlation spectroscopy of membrane-associated Influenza virus fusion peptide strongly supports a helix-turn-helix motif and two turn conformations. *J. Am. Chem. Soc.* **2009**, *131*, 13228−13229.
(34) Grewe, C.; Beck, A.; Gelderblom, H. R. HIV: early virus-cell interactions. *J Acquir Immune Defic Syndr* **1990**, *3*, 965−974.
(35) Miyauchi, K.; Kim, Y.; Latinovic, O.; Morozov, V.; Melikyan, G. B. HIV enters cells via endocytosis and dynamin-dependent fusion with endosomes. *Cell* **2009**, *137*, 433−444.
(36) Herold, N.; Anders-Osswein, M.; Glass, B.; Eckhardt, M.; Muller, B.; Krausslich, H. G. HIV-1 entry in SupT1-R5, CEM-ss, and primary CD4(+) T Cells occurs at the plasma membrane and does not require endocytosis. *J. Virol.* **2014**, *88*, 13956−13970.
(37) Yang, J.; Gabrys, C. M.; Weliky, D. P. Solid-state nuclear magnetic resonance evidence for an extended beta strand conformation of the membrane-bound HIV-1 fusion peptide. *Biochemistry* **2001**, *40*, 8126−8137.
(38) Sackett, K.; Nethercott, M. J.; Epand, R. F.; Epand, R. M.; Kindra, D. R.; Shai, Y.; Weliky, D. P. Comparative analysis of membrane-associated fusion peptide secondary structure and lipid mixing function of HIV gp41 constructs that model the early pre-hairpin intermediate and final hairpin conformations. *J. Mol. Biol.* **2010**, *397*, 301−315.
(39) Macosko, J. C.; Kim, C. H.; Shin, Y. K. The membrane topology of the fusion peptide region of influenza hemagglutinin determined by spin-labeling EPR. *J. Mol. Biol.* **1997**, *267*, 1139−1148.
(40) Han, X.; Bushweller, J. H.; Cafiso, D. S.; Tamm, L. K. Membrane structure and fusion-triggering conformational change of the fusion domain from influenza hemagglutinin. *Nat. Struct. Biol.* **2001**, *8*, 715−720.
(41) Ge, M.; Freed, J. H. Fusion peptide from influenza hemagglutinin increases membrane surface order: An electron-spin resonance study. *Biophys. J.* **2009**, *96*, 4925−4934.
(42) Lorieau, J. L.; Louis, J. M.; Schwieters, C. D.; Bax, A. pH-triggered, activated-state conformations of the influenza hemagglutinin fusion peptide revealed by NMR. *Proc. Natl. Acad. Sci. U. S. A.* **2012**, *109*, 19994−19999.
(43) Liang, S.; Ratnayake, P. U.; Keinath, C.; Jia, L.; Wolfe, R.; Ranaweera, A.; Weliky, D. P. Efficient fusion at neutral pH by Human Immunodeficiency Virus gp41 trimers containing the fusion peptide and transmembrane domains. *Biochemistry* **2018**, *57*, 1219−1235.
(44) Ranaweera, A.; Ratnayake, P. U.; Ekanayaka, E. A. P.; Declercq, R.; Weliky, D. P. Hydrogen-deuterium exchange supports independent membrane-interfacial fusion peptide and transmembrane domains in subunit 2 of influenza virus hemagglutinin protein, a structured and aqueous-protected connection between the fusion peptide and soluble ectodomain, and the importance of membrane apposition by the trimer-of-hairpins structure. *Biochemistry* **2019**, *58*, 2432−2446.
(45) Yao, H. W.; Hong, M. Conformation and lipid interaction of the fusion peptide of the paramyxovirus PIV5 in anionic and negative-curvature membranes from solid-state NMR. *J. Am. Chem. Soc.* **2014**, *136*, 2611−2624.
(46) Chernomordik, L. V.; Kozlov, M. M. Mechanics of membrane fusion. *Nat. Struct. Mol. Biol.* **2008**, *15*, 675−683.
(47) Larsson, P.; Kasson, P. M. Lipid tail protrusion in simulations predicts fusogenic activity of influenza fusion peptide mutants and conformational models. *PLoS Comput. Biol.* **2013**, *9*, e1002950.
(48) Victor, B. L.; Lousa, D.; Antunes, J. M.; Soares, C. M. Self-assembly molecular dynamics simulations shed light into the interaction of the influenza fusion peptide with a membrane bilayer. *J. Chem. Inf. Model.* **2015**, *55*, 795−805.
(49) Worch, R.; Krupa, J.; Filipek, A.; Szymaniec, A.; Setny, P. Three conserved C-terminal residues of influenza fusion peptide alter its behavior at the membrane interface. *Biochim. Biophys. Acta, Gen. Subj.* **2017**, *1861*, 97−105.
(50) Tristram-Nagle, S.; Chan, R.; Kooijman, E.; Uppamoochikkal, P.; Qiang, W.; Weliky, D. P.; Nagle, J. F. HIV fusion peptide penetrates, disorders, and softens T-cell membrane mimics. *J. Mol. Biol.* **2010**, *402*, 139−153.
(51) Légaré, S.; Lagüe, P. The influenza fusion peptide promotes lipid polar head intrusion through hydrogen bonding with phosphates and N-terminal membrane insertion depth. *Proteins: Struct., Funct., Genet.* **2014**, *82*, 2118−2127.
(52) Koynova, R.; Caffrey, M. Phases and phase transitions of the phosphatidylcholines. *Biochim. Biophys. Acta, Rev. Biomembr.* **1998**, *1376*, 91−145.
(53) Mayer, C.; Muller, K.; Weisz, K.; Kothe, G. Deuteron NMR relaxation studies of phospholipid membranes. *Liq. Cryst.* **1988**, *3*, 797−806.
(54) Prosser, R. S.; Davis, J. H.; Mayer, C.; Weisz, K.; Kothe, G. Deuterium NMR relaxation studies of peptide-lipid interactions. *Biochemistry* **1992**, *31*, 9355−9363.
(55) Morrow, M. R.; Simatos, G. A.; Srinivasan, R.; Grandal, N.; Taylor, L.; Keough, K. M. W. The effect of changes in gramicidin conformation on bilayer lipid properties. *Biochim. Biophys. Acta, Biomembr.* **1991**, *1070*, 209−214.
(56) Simatos, G. A.; Forward, K. B.; Morrow, M. R.; Keough, K. M. W. Interaction between perdeuterated dimyristoylphosphatidylcholine and low molecular-weight pulmonary surfactant protein SP-C. *Biochemistry* **1990**, *29*, 5807−5814.
(57) Morrow, M. R.; Stewart, J.; Taneva, S.; Dico, A.; Keough, K. M. W. Perturbation of DPPC bilayers by high concentrations of pulmonary surfactant protein SP-B. *Eur. Biophys. J.* **2004**, *33*, 285−290.
(58) Gabrys, C. M.; Yang, R.; Wasniewski, C. M.; Yang, J.; Canlas, C. G.; Qiang, W.; Sun, Y.; Weliky, D. P. Nuclear magnetic resonance evidence for retention of a lamellar membrane phase with curvature in the presence of large quantities of the HIV fusion peptide. *Biochim. Biophys. Acta, Biomembr.* **2010**, *1798*, 194−201.
(59) Pauls, K. P.; Mackay, A. L.; Soderman, O.; Bloom, M.; Tanjea, A. K.; Hodges, R. S. Dynamic properties of the backbone of an integral membrane polypeptide measured by ^{2}H-NMR. *Eur. Biophys. J.* **1985**, *12*, 1−11.
(60) Meier, P.; Ohmes, E.; Kothe, G. Multipulse dynamic nuclear magnetic resonance of phospholipid membranes. *J. Chem. Phys.* **1986**, *85*, 3598−3614.
(61) Oradd, G.; Lindblom, G. NMR studies of lipid lateral diffusion in the DMPC/gramicidin D/water system: Peptide aggregation and obstruction effects. *Biophys. J.* **2004**, *87*, 980−987.
(62) Davis, J. H.; Ziani, L.; Schmidt, M. L. Critical fluctuations in DOPC/DPPC-d_{62}/cholesterol mixtures: ^{2}H magnetic resonance and relaxation. *J. Chem. Phys.* **2013**, *139*, No. 045104.
(63) Warner, M. Theory of light scattering from vesicles. *Colloid Polym. Sci.* **1983**, *261*, 508−519.

https://doi.org/10.1021/acs.biochem.1c00316
Biochemistry 2021, 60, 2637−2651

(64) Han, X.; Tamm, L. K. A host-guest system to study structure-function relationships of membrane fusion peptides. *Proc. Natl. Acad. Sci. U. S. A.* **2000**, *97*, 13097−13102.
(65) Pereira, F. B.; Goni, F. M.; Muga, A.; Nieva, J. L. Permeabilization and fusion of uncharged lipid vesicles induced by the HIV-1 fusion peptide adopting an extended conformation: dose and sequence effects. *Biophys. J.* **1997**, *73*, 1977−1986.
(66) Yang, R. Synthesis, enhanced fusogenicity, and solid state NMR measurements of oligomeric HIV-1 fusion peptide constructs. Ph. D. dissertation, Michigan State University, East Lansing, MI, 2005.
(67) Brice, A. R.; Lazaridis, T. Structure and dynamics of a fusion peptide helical hairpin on the membrane surface: Comparison of molecular simulations and NMR. *J. Phys. Chem. B* **2014**, *118*, 4461−4470.
(68) Jia, L. H.; Liang, S.; Sackett, K.; Xie, L.; Ghosh, U.; Weliky, D. P. REDOR solid-state NMR as a probe of the membrane locations of membrane-associated peptides and proteins. *J. Magn. Reson.* **2015**, *253*, 154−165.
(69) Baylon, J. L.; Tajkhorshid, E. Capturing spontaneous membrane insertion of the Influenza virus Hemagglutinin fusion peptide. *J. Phys. Chem. B* **2015**, *119*, 7882−7893.
(70) Lai, A. L.; Freed, J. H. HIV gp41 fusion peptide increases membrane ordering in a cholesterol-dependent fashion. *Biophys. J.* **2014**, *106*, 172−181.
(71) Chakraborty, H.; Lentz, B. R.; Kombrabail, M.; Krishnamoorthy, G.; Chattopadhyay, A. Depth-dependent membrane ordering by Hemagglutinin fusion peptide promotes fusion. *J. Phys. Chem. B* **2017**, *121*, 1640−1648.
(72) Heller, W. T.; Zolnierczuk, P. A. The helix-to-sheet transition of an HIV-1 fusion peptide derivative changes the mechanical properties of lipid bilayer membranes. *Biochim. Biophys. Acta, Biomembr.* **2019**, *1861*, 565−572.
(73) Tristram-Nagle, S.; Nagle, J. F. HIV-1 fusion peptide decreases bending energy and promotes curved fusion intermediates. *Biophys. J.* **2007**, *93*, 2048−2055.

https://doi.org/10.1021/acs.biochem.1c00316
Biochemistry 2021, 60, 2637−2651

Supporting Information for Publication

Rapid ^{2}H NMR transverse relaxation of perdeuterated lipid acyl chains of membrane with bound viral fusion peptide supports large-amplitude motions of these chains that can catalyze membrane fusion

Ujjayini Ghosh and David P. Weliky *, Department of Chemistry, Michigan State University, East Lansing, MI, 48824

Figure S1. Fitted relaxation rates of DMPC-d54. For all tables, fitting uncertainties are given in parentheses. For a sample and temperature, the first -C^2H_2 rate is also given in Table 1 and Figs. 4 and 5 in the main manuscript and is typically for the most intense region of the -C^2H_2 spectrum that does not overlap with the -C^2H_3 signals. The inner and outer -C^2H_2 integration ranges discussed in the text and Fig. 6 of the main manuscript are respectively closer and further from the central integration range used to determine -C^2H_3 intensity. Spectra are typically for τ = 63 μs. The peptide:DMPC-d54 mole ratio = 1:25.

35 C

No peptide

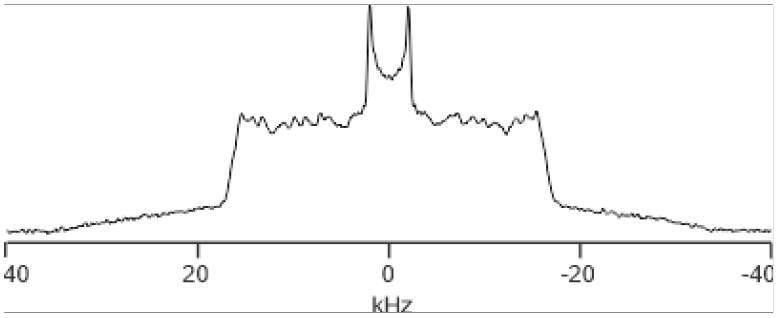

Group	Rate, s^{-1}	Integration range, kHz
-C^2H_2	951(6)	{[12 → 17] + [-12 → -17]} – {[19 → 24] + [-19 → -24]}
-C^2H_2	902(10)	{[5 → 7.5] + [-5 → -7.5]} – 0.5 × {[19 → 24] + [-19 → -24]}
-C^2H_3	313(9)	{[2.5 → -2.5]} – {[5 → 7.5] + [-5 → -7.5]}

GPfp

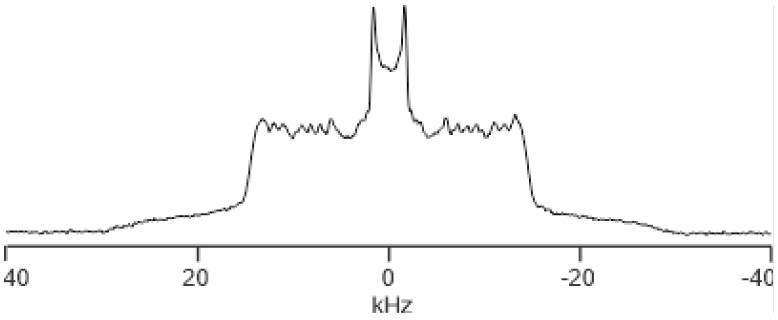

Group	Rate, s^{-1}	Integration range, kHz
-C^2H_2	1147(7)	{[10 → 15] + [-10 → -15]} – {[17 → 22] + [-17 → -22]}
-C^2H_2	1125(35)	{[5 → 7.5] + [-5 → -7.5]} – 0.5 × {[17 → 22] + [-17 → -22]}
-C^2H_3	392(5)	{[2.5 → -2.5]} – {[5 → 7.5] + [-5 → -7.5]}

HAfp, pH 7

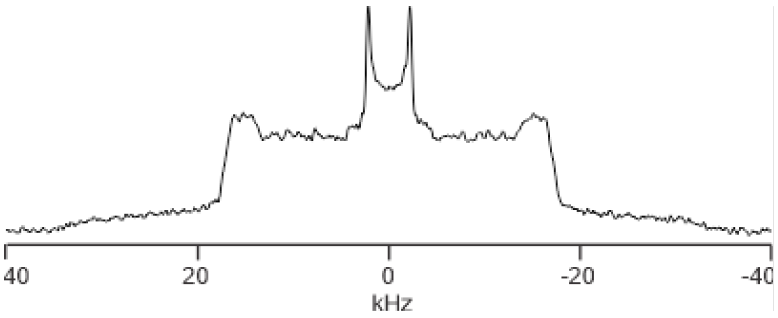

Group	Rate, s^{-1}	Integration range, kHz
-C^2H_2	1290(15)	{[13 → 18] + [-13 → -18]} – {[20 → 25] + [-20 → -25]}
-C^2H_2	1223(47)	{[5 → 7.8] + [-5 → -7.8]} – 0.56 × {[20 → 25] + [-20 → -25]}
-C^2H_3	477(13)	{[2.8 → -2.8]} – {[5 → 7.8] + [-5 → -7.8]}

HAfp, pH 5

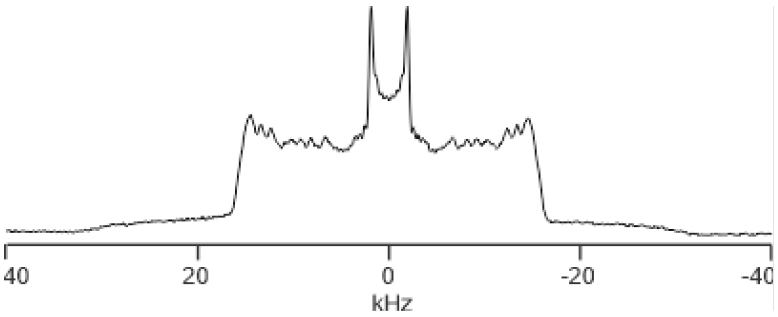

Group	Rate, s^{-1}	Integration range, kHz
-C^2H_2	1110(11)	{[12 → 17] + [-12 → -17]} – {[18 → 23] + [-18 → -23]}
-C^2H_2	1181(30)	{[5 → 7.5] + [-5 → -7.5]} – 0.5 × {[18 → 23] + [-18 → -23]}
-C^2H_3	407(8)	{[2.5 → -2.5]} – {[5 → 7.5] + [-5 → -7.5]}

30 C

No peptide

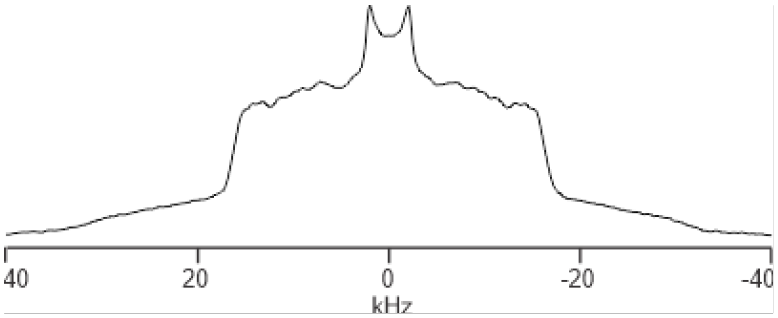

Group	Rate, s^{-1}	Integration range, kHz
$-C^2H_2$	950(9)	{[12 → 17] + [-12 → -17]} – {[19 → 24] + [-19 → -24]}
$-C^2H_2$	858(7)	{[5 → 7.5] + [-5 → -7.5]} – 0.5 × {[19 → 24] + [-19 → -24]}
$-C^2H_3$	334(8)	{[2.5 → -2.5]} – {[5 → 7.5] + [-5 → -7.5]}

GPfp

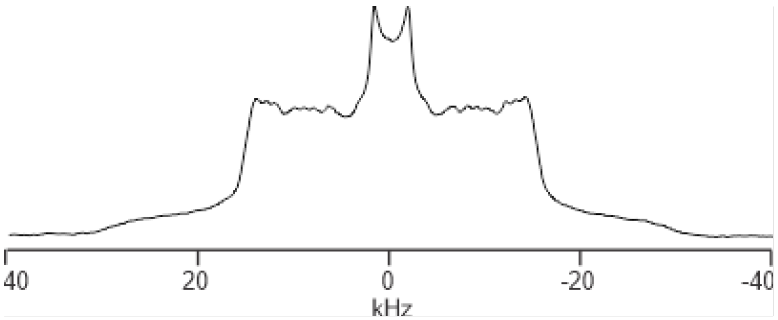

Group	Rate, s^{-1}	Integration range, kHz
$-C^2H_2$	1096(10)	{[11 → 16] + [-11 → -16]} – {[21 → 26] + [-21 → -26]}
$-C^2H_2$	968(20)	{[5 → 7.5] + [-5 → -7.5]} – {[21 → 26] + [-21 → -26]}
$-C^2H_3$	407(4)	{[2.5 → -2.5]} – {[5 → 7.5] + [-5 → -7.5]}

HAfp, pH 7

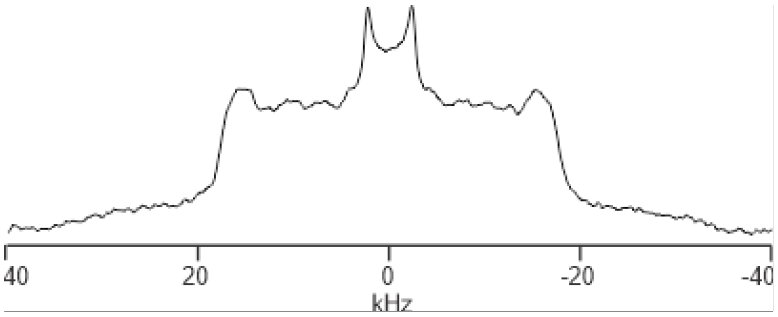

Group	Rate, s^{-1}	Integration range, kHz
$-C^2H_2$	1518(35)	{[12 → 18] + [-12 → -18]} – {[24 → 30] + [-24 → -30]}
$-C^2H_2$	1261(25)	{[6 → 8.8] + [-6 → 8.8]} – 0.47 × {[24 → 30] + [-24 → -30]}
$-C^2H_3$	512(34)	{[2.8 → -2.8]} – {[6 → 8.8] + [-6 → 8.8]}

HAfp, pH 5

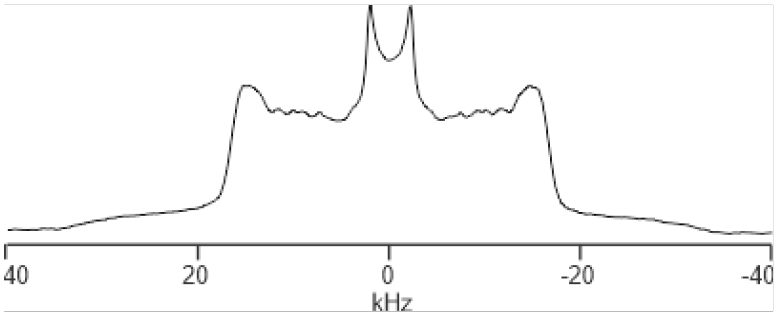

Group	Rate, s^{-1}	Integration range, kHz
$-C^2H_2$	1255(12)	{[12 → 17] + [-12 → -17]} – {[21 → 26] + [-21 → -26]}
$-C^2H_2$	1318(24)	{[6 → 8.6] + [-6 → -8.6]} – 0.52 × {[21 → 26] + [-21 → -26]}
$-C^2H_3$	413(12)	{[2.6 → -2.6]} – {[6 → 8.6] + [-6 → -8.6]}

25 C

No peptide

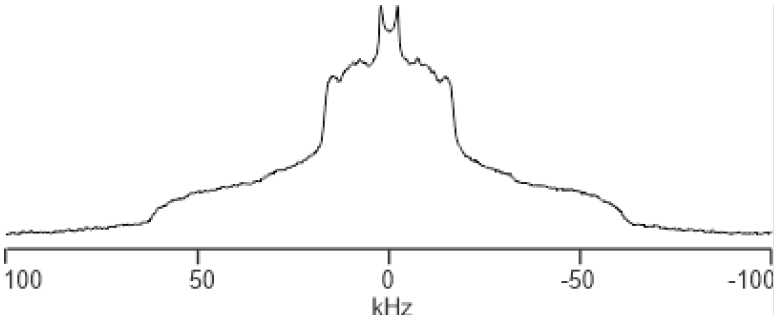

Group	Rate, s^{-1}	Integration range, kHz
$-C^2H_2$	1078(23)	{[12 → 17] + [-12 → -17]} – {[19 → 24] + [-19 → -24]}
$-C^2H_2$	966(19)	{[5 → 7.5] + [-5 → -7.5]} – 0.5 × {[19 → 24] + [-19 → -24]}
$-C^2H_3$	316(9)	{[2.5 → -2.5]} – {[5 → 7.5] + [-5 → -7.5]}

GPfp

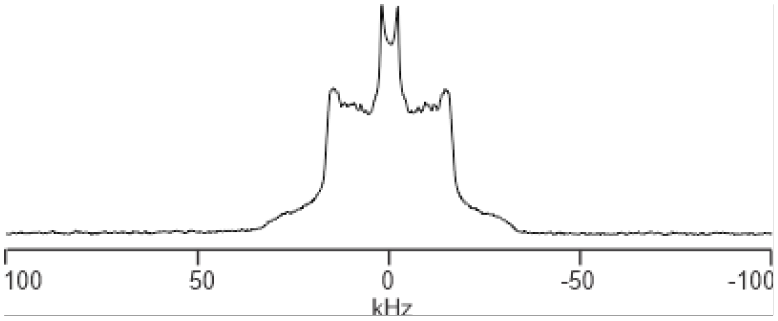

Group	Rate, s^{-1}	Integration range, kHz
$-C^2H_2$	1025(20)	{[12 → 17] + [-12 → -17]} – {[21 → 26] + [-21 → -26]}
$-C^2H_2$	1073(27)	{[6→ 8.6] + [-6 → -8.6]} – {[21 → 26] + [-21 → -26]}
$-C^2H_3$	418(4)	{[2.6 → -2.6]} – {[6→ 8.6] + [-6 → -8.6]}

HAfp, pH 7

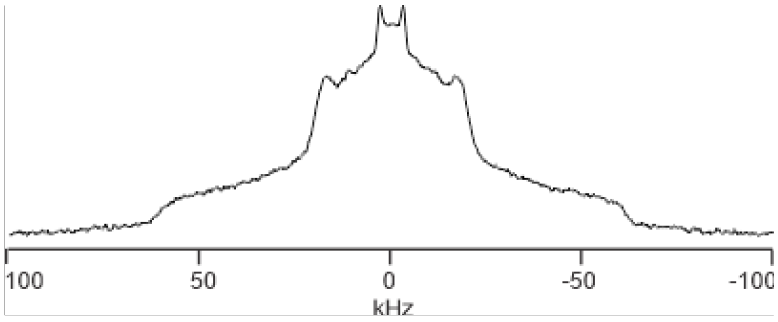

Group	Rate, s^{-1}	Integration range, kHz
$-C^2H_2$	2116(53)	{[15 → 21] + [-15 → -21]} – {[30 → 36] + [-30 → -36]}
$-C^2H_2$	1355(26)	{[7 → 11] + [-7 → -11]} – 0.67 × {[30 → 36] + [-30 → -36]}
$-C^2H_2$	1759(41)	{[30 → 36] + [-30 → -36]} – {[66 → 72] + [-66 → -72]}
$-C^2H_3$	609(25)	{[4 → -4]} – {[7 → 11] + [-7 → -11]}

HAfp, pH 5

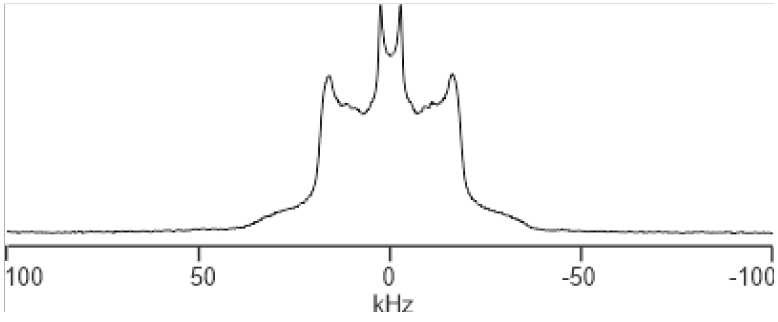

Group	Rate, s^{-1}	Integration range, kHz
$-C^2H_2$	1864(27)	{[13.3 → 19.3] + [-13.3 → -19.3]} – {[25 → 31] + [-25 → -31]}
$-C^2H_2$	1742(16)	{[6 → 9] + [-6 → -9]} – {[25 → 31] + [-25 → -31]}
$-C^2H_3$	516(8)	{[3.25 → -3.25]} – 1.08 × {[6 → 9] + [-6 → -9]}

20 C

No peptide

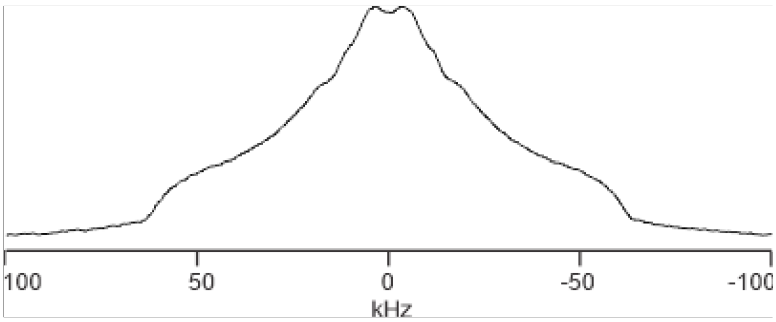

Group	Rate, s^{-1}	Integration range, kHz
$-C^2H_2$	1878(33)	{[15 → 25] + [-15 → -25]}
$-C^2H_2$	2095(49)	{[35 → 45] + [-35 → -45]}
$-C^2H_3$	1009(15)	{[10 → -10]} – {[15 → 25] + [-15 → -25]}

GPfp

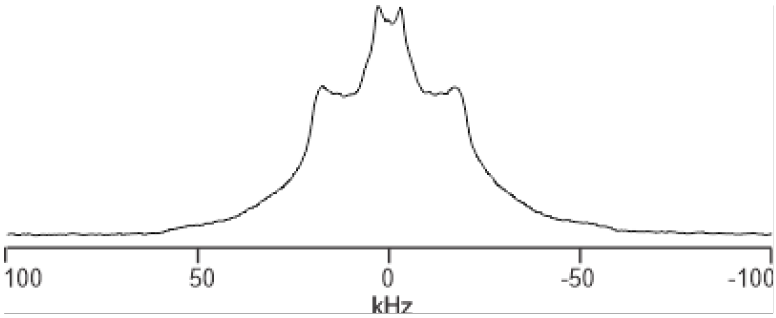

Group	Rate, s^{-1}	Integration range, kHz
$-C^2H_2$	$R_{2,f}$ = 9480(918) s^{-1}, A_f = 0.660(16), $R_{2,s}$ = 1782(59) s^{-1}, A_s = 0.340(19)	{[15 → 21] + [-15 → -21]} – {[30 → 36] + [-30 → -36]}
$-C^2H_2$	$R_{2,f}$ = 8533(1069) s^{-1}, A_f = 0.697(17), $R_{2,s}$ = 1644(107) s^{-1}, A_s = 0.303(32)	{[8 → 12] + [-8 → -12]} – 0.67 × {[30→36] + [-30→-36]}
$-C^2H_3$	928(32)	{[4 → -4]} – {[8 → 12] + [-8 → -12]}

HAfp, pH 7

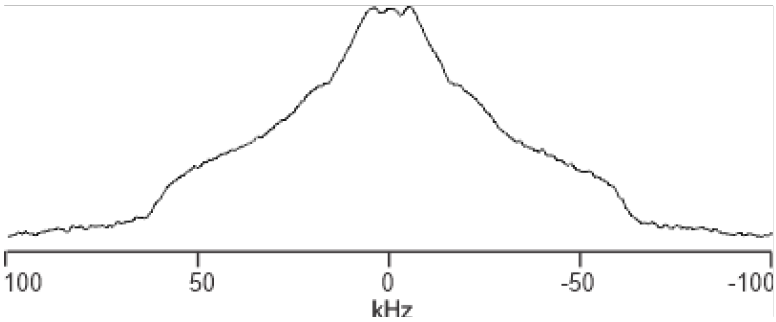

Group	Rate, s^{-1}	Integration range, kHz
$-C^2H_2$	1935(40)	{[25 → 35] + [-25 → -35]}
$-C^2H_2$	2267(115)	{[50 → 60] + [-50 → -60]}
$-C^2H_3$	1177(29)	{[10 → -10]} – {[25 → 35] + [-25 → -35]}

HAfp, pH 5

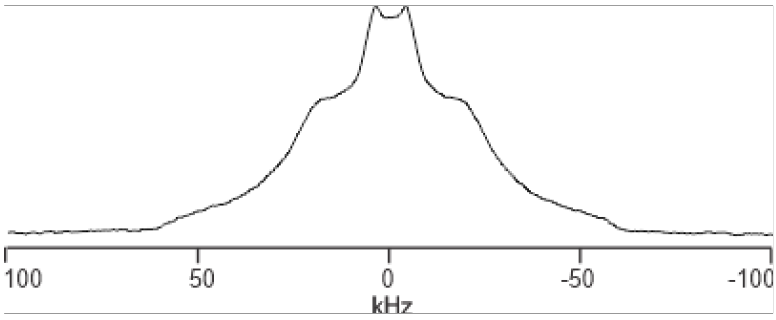

Group	Rate, s^{-1}	Integration range, kHz
$-C^2H_2$	$R_{2,f}$ = 14088(374) s^{-1}, A_f = 0.965(17), $R_{2,s}$ = 876(163) s^{-1}, A_s = 0.035(4)	{[16 → 26] + [-16 → -26]}
$-C^2H_2$	$R_{2,f}$ = 7818(846) s^{-1}, A_f = 0.877(33), $R_{2,s}$ = 918(465) s^{-1}, A_s = 0.123(46)	{[40 → 50] + [-40 → -50]}
$-C^2H_3$	2745(92)	{[8 → -8]} – 0.8 ×{[16 → 26]+[-16 → -26]}

10 C

No peptide

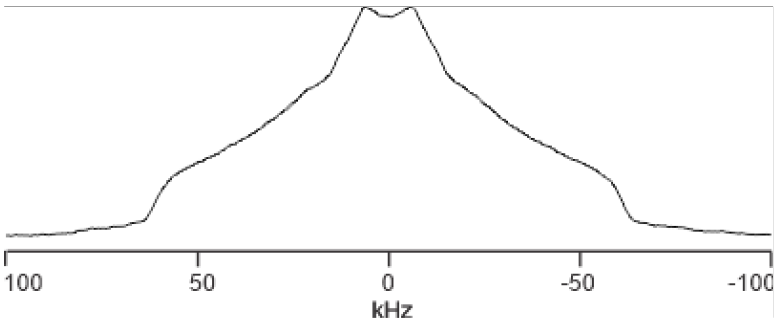

Group	Rate, s^{-1}	Integration range, kHz
$-C^2H_2$	2136(22)	{[15 → 25] + [-15 → -25]}
$-C^2H_2$	2432(50)	{[35 → 45] + [-35 → -45]}
$-C^2H_3$	1194(10)	{[10 → -10]} – {[15 → 25] + [-15 → -25]}

GPfp

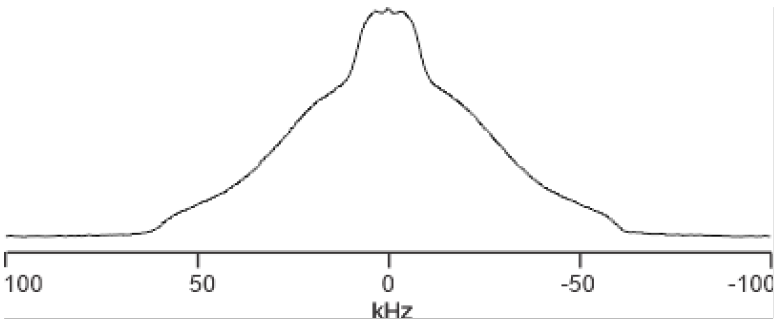

Group	Rate, s^{-1}	Integration range, kHz
$-C^2H_2$	7030(127)	{[15 → 25] + [-15 → -25]}
$-C^2H_2$	6380(194)	{[35 → 45] + [-35 → -45]}
$-C^2H_3$	2780(80)	{[10 → -10]} – {[15 → 25] + [-15 → -25]}

HAfp, pH 7

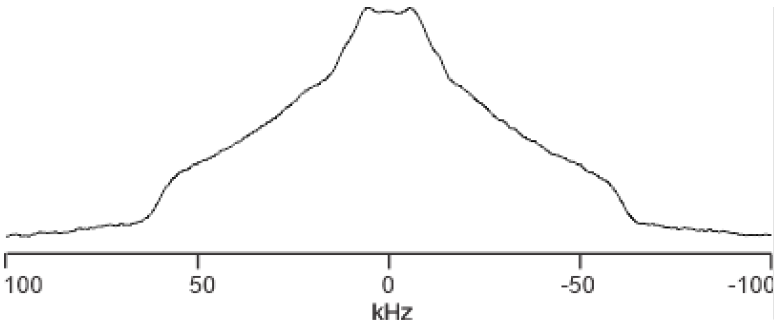

Group	Rate, s^{-1}	Integration range, kHz
$-C^2H_2$	2068(15)	{[15 → 25] + [-15 → -25]}
$-C^2H_2$	2463(71)	{[35 → 45] + [-35 → -45]}
$-C^2H_3$	1085(26)	{[10 → -10]} – {[15 → 25] + [-15 → -25]}

HAfp, pH 5

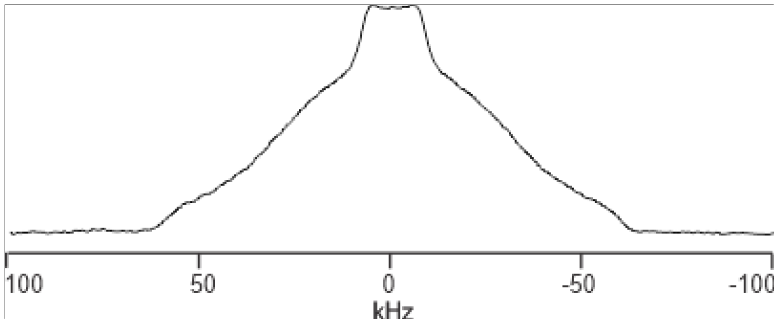

Group	Rate, s^{-1}	Integration range, kHz
$-C^2H_2$	4347(131)	{[15 → 25] + [-15 → -25]}
$-C^2H_2$	4411(205)	{[35 → 45] + [-35 → -45]}
$-C^2H_3$	2505(106)	{[10 → -10]} – {[15 → 25] + [-15 → -25]}

0 C

No peptide

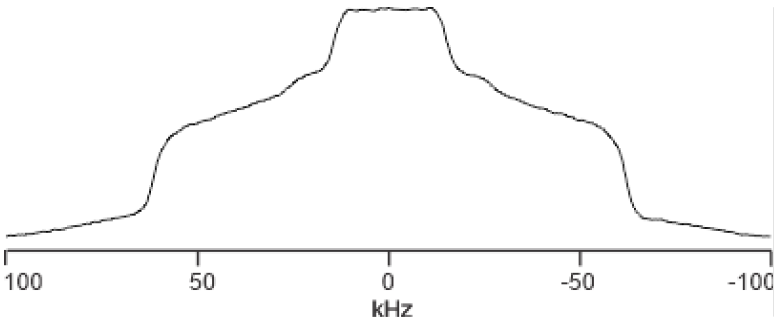

Group	Rate, s^{-1}	Integration range, kHz
$-C^2H_2$	2994(64)	{[47 → 63] + [-47 → -63]}
$-C^2H_2$	2668(111)	{[73 → 89] + [-73 → -89]}
$-C^2H_3$	1548(25)	{[16 → -16]} – {[73 → 89] + [-73 → -89]}

GPfp

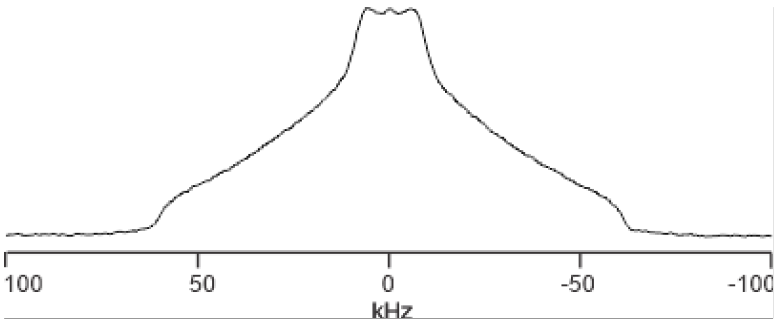

Group	Rate, s^{-1}	Integration range, kHz
$-C^2H_2$	4078(141)	{[25 → 40] + [-25 → -40]}
$-C^2H_2$	3613(86)	{[46 → 61] + [-46 → -61]}
$-C^2H_3$	1736(68)	{[10 → -10]} – 0.67 × {[25 → 40] + [-25 → -40]}

HAfp, pH 7

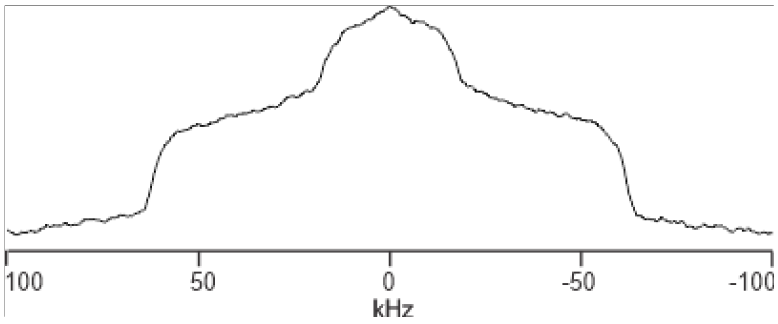

Group	Rate, s^{-1}	Integration range, kHz
$-C^2H_2$	2772(64)	{[45 → 63] + [-45 → -63]}
$-C^2H_2$	2353(96)	{[73 → 91] + [-73 → -91]}
$-C^2H_3$	1710(28)	{[18 → -18]}

HAfp, pH 5

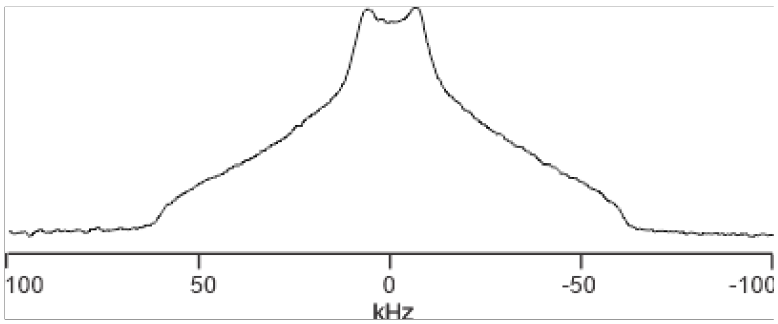

Group	Rate, s^{-1}	Integration range, kHz
$-C^2H_2$	4286(118)	{[25 → 40] + [-25 → -40]}
$-C^2H_2$	3721(90)	{[45 → 60] + [-45 → -60]}
$-C^2H_3$	1409(42)	{[10 → -10]} – 0.67 × {[25 → 40] + [-25 → -40]}

Figure S2. Fitted transverse relaxation rates for DMPC-d54 with HAfp, pH 7 at HAfp:DMPC-d54 mole ratio = 1:50. For all tables, fitting uncertainties are given in parentheses. Spectra are for τ = 63 μs.

35 C

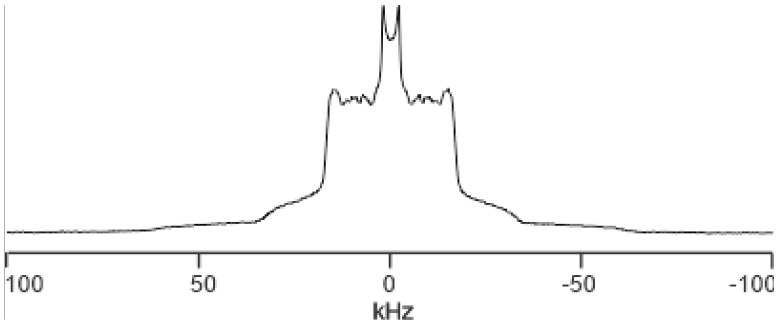

Group	Rate, s^{-1}	Integration range, kHz
$-C^2H_2$	1363(27)	{[12 → 20] + [-12 → -20]} – {[38 → 46] + [-38 → -46]}
$-C^2H_2$	1274(20)	{[4 → 12] + [-4 → -12]} – {[38 → 46] + [-38 → -46]}
$-C^2H_2$	1959(39)	{[20 → 28] + [-20 → -28]} – {[38 → 46] + [-38 → -46]}
$-C^2H_3$	437(8)	{[4 → -4]} – 0.5 × {[4 → 12] + [-4 → -12]}

30 C

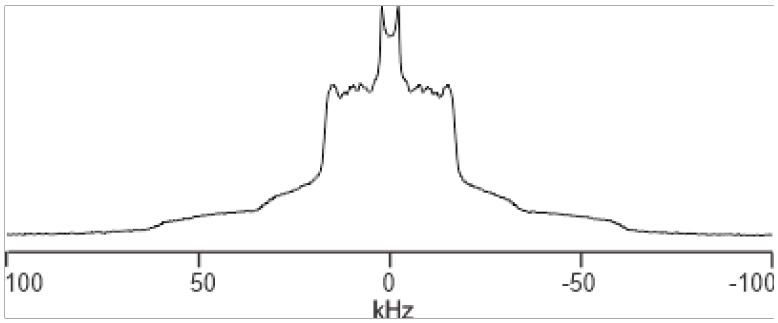

Group	Rate, s^{-1}	Integration range, kHz
$-C^2H_2$	1438(23)	{[12 → 20] + [-12 → -20]} – {[39 → 47] + [-39 → -47]}
$-C^2H_2$	1200(13)	{[4 → 12] + [-4 → -12]} – {[39 → 47] + [-39 → -47]}
$-C^2H_2$	1738(47)	{[22 → 30] + [-22 → -30]} – {[39 → 47] + [-39 → -47]}
$-C^2H_3$	398(5)	{[4 → -4]} – 0.5 × {[4 → 12] + [-4 → -12]}

25 C

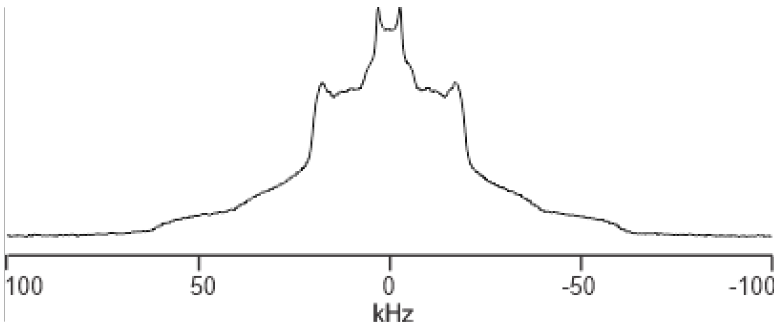

Group	Rate, s^{-1}	Integration range, kHz
$-C^2H_2$	1962(39)	{[16 → 24] + [-16 → -24]} – {[43 → 51] + [-43 → -51]}
$-C^2H_2$	1843(34)	{[8 → 16] + [-8 → -16]} – {[43 → 51] + [-43 → -51]}
$-C^2H_2$	2120(92)	{[25 → 33] + [-25 → -33]} – {[43 → 51] + [-43 → -51]}
$-C^2H_3$	682(24)	{[8 → -8]} – {[8 → 16] + [-8 → -16]}

20 C

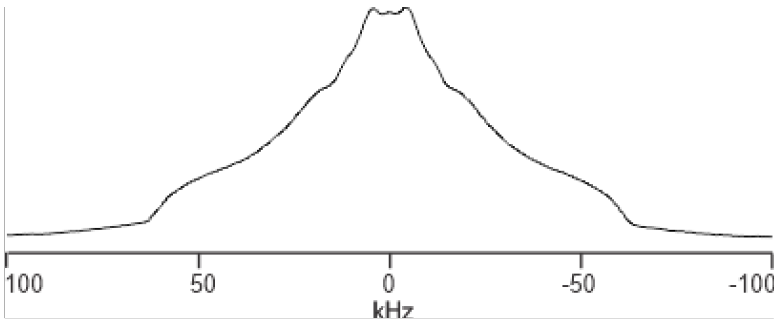

Group	Rate, s^{-1}	Integration range, kHz
$-C^2H_2$	2250(75)	{[10 → 20] + [-10 → -20]}
$-C^2H_2$	2529(109)	{[21 → 31] + [-21 → -31]}
$-C^2H_2$	2697(160)	{[48 → 58] + [-48 → -58]}
$-C^2H_2$	2225(139)	{[68 → 78] + [-68 → -78]}
$-C^2H_3$	1257(35)	{[10 → -10]} – {[10 → 20] + [-10 → -20]}

10 C

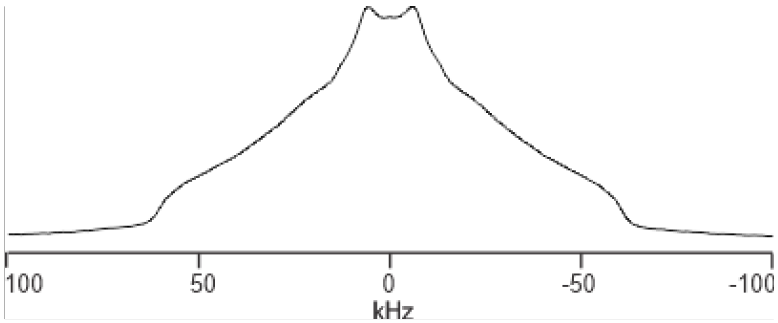

Group	Rate, s^{-1}	Integration range, kHz
$-C^2H_2$	2509(72)	{[12 → 24] + [-12 → -24]}
$-C^2H_2$	2422(74)	{[25 → 37] + [-25 → -37]}
$-C^2H_3$	947(25)	{[12 → -12]} – {[12 → 24] + [-12 → -24]}
$-C^2H_3$	1345(30)	{[12 → -12]} – {[25 → 37] + [-25 → -37]}

Figure S3. Bar plots of temperature-dependent outer (dotted) and inner (cross hatch) -C^2H_2 NMR transverse relaxation rates of DMPC-d54 without peptide and with peptide for peptide:DMPC-d54 molar ratio = 1:25. The rates and their uncertainties are numerically presented in Figure S1, as are the "outer" and "inner" spectral frequency ranges for integration. These ranges are typically different for different samples and temperatures because of the large dependences of spectral lineshapes and linewidths on sample and temperature. The outer and inner ranges are both outside of the interval defined by 2× the peak splitting of the -C^2H_3 horns, so as to not include -C^2H_3 intensity in the integration (Fig. 3A). For GPfp and HAfp, pH 5 at 20 °C, the displayed bars are for the dominant fast rates of the bi-exponential decays. To reduce the vertical space of the figure, these 20 °C bar heights are respectively 0.9× and 0.6× the true rates presented in Fig. S1.

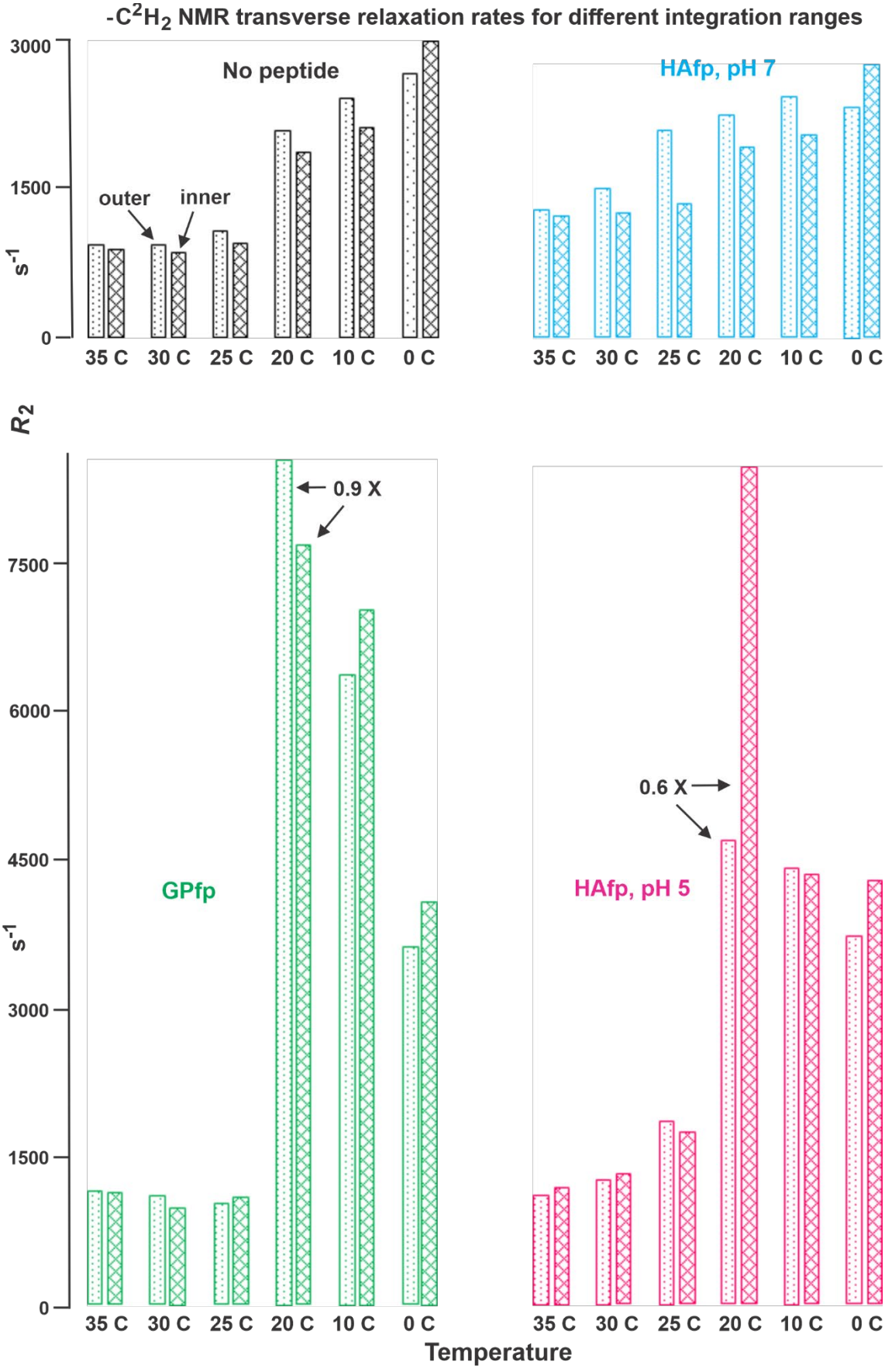
-C2H2 NMR transverse relaxation rates for different integration ranges
No peptide
HAfp, pH 7
outer
inner
R2
s-1
3000
1500
0
35 C
30 C
25 C
20 C
10 C
0 C
0.9 X
0.6 X
GPfp
HAfp, pH 5
7500
6000
4500
3000
1500
0
Temperature